COMPLIANT MICROSTRUCTURES FOR ENHANCED THERMAL CONDUCTANCE ACROSS INTERFACES

by

Jin Cui

A Dissertation

Submitted to the Faculty of Purdue University

In Partial Fulfillment of the Requirements for the degree of

Doctor of Philosophy

School of Mechanical Engineering

West Lafayette, Indiana

August 2020

THE PURDUE UNIVERSITY GRADUATE SCHOOL
STATEMENT OF COMMITTEE APPROVAL

Dr. Liang Pan, Co-chair

School of Mechanical Engineering

Dr. Justin Weibel, Co-chair

School of Mechanical Engineering

Dr. Jun Chen

School of Mechanical Engineering

Dr. Tongcang Li

Department of Physics and Astronomy

Approved by:

Dr. Nicole L. Key

Dedicated to my parents, Jixun Cui and Yujie Yin, and my aunt, Min Cui

ACKNOWLEDGMENTS

First of all, I would like to thank my advisors, Prof. Liang Pan and Prof. Justin Weibel, for their help and guidance during my PhD study. They have been supportive all the time since I got admittance to the PhD program. They have put a lot of their time and resources into my project. I have derived a good deal of benefit from their invaluable discussion and advice. I would like to thank members of the Cooling Technologies Research Center (CTRC), a graduated National Science Foundation (NSF) Industry/University Cooperative Research Center at Purdue University, and the National Science Foundation for their financial support for my project. I would like to acknowledge Prof. Jun Chen and Prof. Tongcang Li for their help and serving as my committee members. I would also like to thank Prof. Suresh Garimella, for his enduring support and valuable suggestions.

I would like to express my gratitude and appreciation to all the group members I have been working with, Chen Chen, Zhidong Du, Qiming Chen, Shih-Hsin Hsu, Bojing Yao, Ivel Collins, Serdar Ozguc, Xuemei Chen, Srivathsan Sudhakar, Rishav Roy, Aaditya Candadai, and many more. Their productive discussion and warm accompany makes my Ph.D. study a wonderful experience.

Finally, I would like to offer my ultimate gratitude to my family, especially my parents and my Aunt Min. Without their encouragement and support, I will never succeed to finish my Ph.D. study.

TABLE OF CONTENTS

LIST OF FIGURES

ABSTRACT

With the extreme increases in power density of electronic devices, the contact thermal resistance imposed at interfaces between mating solids becomes a major challenge in thermal management. This contact thermal resistance is mainly caused by micro-scale surface asperities (roughness) and wavy profile of surface (nonflatness) which severely reduce the contact area available for heat conduction. High contact pressures (1~100 MPa) can be used to deform the surface asperities to increase contact area. Besides, a variety of conventional thermal interface materials (TIM), such as greases and pastes, are used to improve the contact thermal conductance by filling the remaining air gaps. However, there are still some applications where such TIMs are disallowed for reworkability concerns. For example, heat must be transferred across dry interfaces to a heat sink in pluggable opto-electronic transceivers which needs to repeatedly slide into / out of contact with the heat sink. Dry contact and low contact pressures are required for this sliding application.

This dissertation presents a metallized micro-spring array as a surface coating to enhance dry contact thermal conductance under ultra-low interfacial contact pressure. The shape of the micro-springs is designed to be mechanically compliant to achieve conformal contact between nonflat surfaces. The polymer scaffolds of the micro-structured TIMs are fabricated by using a custom projection micro-stereolithography (μSL) system. By applying the projection scheme, this method is more cost-effective and high-throughput than other 3D micro-fabrication methods using a scanning scheme. The thermal conductance of polymer micro-springs is further enhanced by metallization using plating and surface polishing on their top surfaces. The measured mechanical compliance of TIMs indicates that they can deform ~10s μm under ~10s kPa contact pressures over their footprint area, which is large enough to accommodate most of surface nonflatness of electronic packages. The measured thermal resistances of the TIM at different fabrication stages confirms the enhanced thermal conductance by applying metallization and surface polishing. Thermal resistances of the TIMs are compared to direct metal-to-metal contact thermal resistance for flat and nonflat mating surfaces, which confirms that the TIM outperforms direct contact. A thin layer of soft polymer is coated on the top surfaces of the TIMs to accommodate surface roughness that has a smaller spatial period than the micro-springs. For rough surfaces, the polymer-

coated TIM has reduced thermal resistance which is comparable to a benchmark case where the top surfaces of the TIM are glued to the mating surface. A polymer base is designed under the micro-spring array which can provide the advantages for handling as a standalone material or integration convenience, at the toll of an increased insertion resistance. Through-holes are designed in the base layer and coated with thermally conductive metal after metallization to enhance thermal conductance of the base layer; a thin layer of epoxy is applied between the base layer and the working surface to reduce contact thermal resistance exposed on the base layer. Cycling tests are conducted on the TIMs; the results show good early-stage reliability of the TIM under normal pressure, sliding contact, and temperature cycles. The TIM is thermally demonstrated on a pluggable application, namely, a CFP4 module, which shows enhanced thermal conductance by applying the TIM.

To further enhance the potential mechanical compliance of microstructured surfaces, a stable double curved beam structure with near-zero stiffness composed of intrinsic negative and positive stiffness elastic elements is designed and fabricated by introducing residual stresses. Stiffness measurements shows that the positive-stiffness single curved beam, which is the same as the top beam in the double curved beam, is stiffer than the double curved beam, which confirms the negative stiffness of the bottom beam in the double curved beam. Layered near zero-stiffness materials made of these structures are built to demonstrate the scalability of the zero-stiffness zone.

1. INTRODUCTION

The continuous miniaturization of electronic devices causes extreme increases in power density which call for new thermal management technologies to main the devices at a reliable operating temperature [1-3]. The parasitic contact thermal resistances across solid-to-solid interfaces contribute significantly to the overall resistance for heat rejection.

1.1 Contact Thermal Resistance

Real surfaces have imperfections like microscale surface asperities (roughness) and wavy surface profile (nonflatness) as shown in Figure 1.1 (a). When a heat generation device contacts a heat sink, the shape mismatching of the imperfections on the mating surfaces dramatically reduces the contact area (1-2% of apparent area) and leaves voids between the surfaces, which seriously jeopardizes heat rejection [4-9]. As shown in Figure 1.1 (b), there is a sudden temperature drop (ΔT) cross the interface. The concept of thermal resistance is applied to characterize this interfacial effect, which is called contact thermal resistance (R_c).

$$R_c = \frac{\Delta T}{Q}$$

where Q is the heat flux across the interface. There are several methods developed to enhance contact thermal conductance. One kind of solution is to compress the two surfaces with a large pressure to deform the asperities and fill the air gaps. To enhance contact thermal conductance, the compressive pressures typically need to be 1-100s MPa or even larger for metal-to-metal contact [10-12]. Another solution is to fill the air gaps with flowable or soft materials, like greases and pads, to increase the contact areas, which are so-called thermal interface materials (TIMs) [7-9].

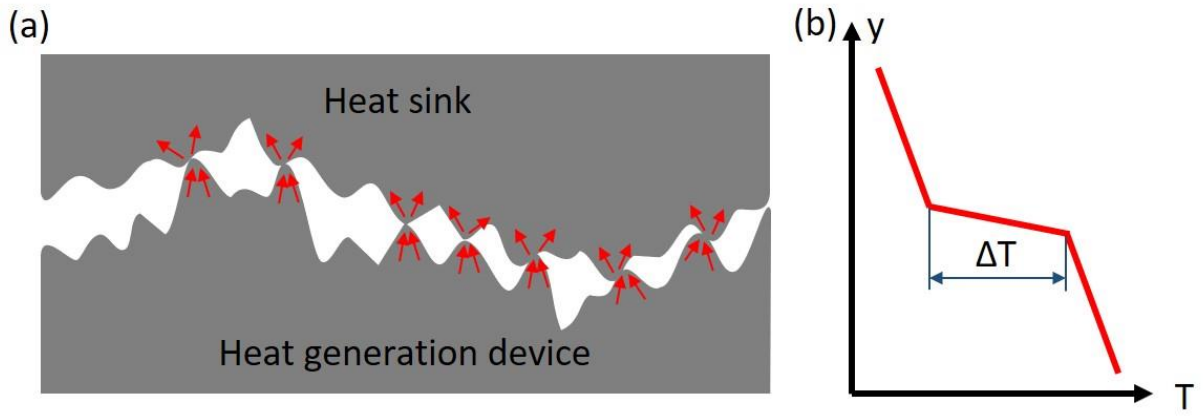

Figure 1.1. (a) Schematic illustration of the interface between a heat generation device and heat sink; the red arrows indicate the heat flow across the interface. (b) Temperature profile near the interface; ΔT indicates the sudden temperature drop across the interface.

1.2 Thermal Interface Materials (TIMs)

Thermal interface materials are thermally conductive materials which are mechanically compliant or flowable and can fill the voids at the interface to increase effective contact area. An ideal TIM only fill the existing voids between surfaces. However, a real TIM generates gaps between surfaces even if it is highly compliant or flowable [7-8]. The gap generated by TIM is treated as the effective thickness of TIM which is called the bond line thickness (BLT). The thermal interfacial resistance for a TIM (R_{TIM}) can be characterized by BLT as [8, 9, 12, 13]

$$R_{TIM} = R_{c1} + \frac{BLT}{k_{TIM}} + R_{c2}$$

R_{c1} and R_{c2} are contact thermal resistances imposed at the interfaces between TIM and two mating surfaces. k_{TIM} is thermal conductivity of TIM. From the equation, there are three ways to reduce R_{TIM}: reduce R_c, reduce BLT and increase k_{TIM}. R_c depends on how well the TIM conforms to and wets the surfaces, which is related to the mechanical compliance and flowability of TIM, as well as compressive pressures. BLT is directly related to the amount of the TIM. Typically, less BLT means less materials, less cost and less thermal resistance which is desirable, but too little BLT is not enough to fill the voids and causes voiding due to the uneven distribution of TIM. For solid materials, BLT is related to mechanical compliance of the TIM and the applied pressure; for

liquid materials, BLT is related to the viscosity of the TIM and clamping pressures. k_{TIM} measures how well the heat can be transferred inside the TIM. k_{TIM} is coupled with BLT to influence RTIM: for TIM with large BLT, k_{TIM} is a critical parameter, while for TIM with small BLT, the influence of k_{TIM} is relatively small.

1.3 Conventional TIMs

Varieties of conventional TIMs [7-9] have been developed and are commercially available. Based on the properties and applications, these TIMs can be generally divided into five types: thermal grease, thermal conductive adhesives (TCAs), solders, thermal pads and phase change materials (PCMs) [9]. Thermal grease is typically flowable silicone or hydrocarbon oil, which conforms to surfaces well. Due to the flowability, thermal grease can form a thin layer with a BLT of 10s μm. To further enhance thermal conductivity, high-thermal-conductivity particles are mixed in the matrix. High-performance thermal grease has thermal resistance as low as 10 $mm^2 \cdot K/W$ [14]. Thermal grease is a widely used TIM, but its reliability is affected by pump-out and dry-out effects which generate voids at the interface [15]. TCAs, like thermal grease, are liquid matrix with thermally conductive particles dispersed inside. Different from thermal grease, the matrix of TCAs is typically an epoxy which is cured after being applied to interfaces. Cured TCAs generate rigid and strong bonds between surfaces, which eliminates pump-out effect, but makes TCAs not replaceable. Solder TIMs are made of alloys with relatively low melting points which reflow under low temperature to fill the voids between surfaces. After being applied, solder TIMs form metallic bond between surfaces which exhibit extremely low thermal resistances (<5 $mm^2 \cdot K/W$) [9] due to its intrinsic high thermal conductivity. However, the high modulus of solder TIMs cause the problem of stress-induced cracking [9]. Voiding during melted metal reflow is also a main concern for solder TIM [8]. Thermal pads are soft solid pads, typically polymer, with thermally conductive particles embedded inside. Due to its solid form, thermal pads are easier to handle and apply and can be reused. However, the BLT of thermal pads is relatively high (~100s – 1000s μm) [15] and a high pressure is required to deform this bulk material to conform to the surfaces. Besides, thermally conductive fillers are typically rigid particles which enhance the thermal conductivity, but meanwhile undermine the mechanical compliance. The tradeoff between mechanical compliance and filling ratio of the particles limits the overall performance of thermal pads. PCMs

[9] consist of matrix which have melting points between room temperature and operating temperature. This property allows PCMs to be easily handled, like pads, and reflow to fill the voids and form thin BLTs when operating, like grease.

1.4 Structured TIMs

An ideal TIM should have high thermal conductivity and high mechanical compliance which makes it a conformal thermally conductive layer inserted between surfaces. However, there is a conflict between thermal conductivity and mechanical compliance for normal materials, because dense and bulk materials typically have high thermal conductivity, but also high stiffness. Therefore, TIMs with engineered nano-/micro-structures [9, 16, 17] are developed which have outstanding thermal performances, compared to conventional TIMs. Polymers matrix can be liquid form for low degree of polymerization, which is flowable, or solid form for high degree of polymerization which have good mechanical compliance. Both kinds of the polymers have mechanical performances suitable for TIMs, but relatively low thermal conductivities (~0.1-0.3 $W/m^{-1}K^{-1}$) [8, 9]. To enhance thermal conductivity, polymers are laden with thermally conductive particles, e.g. ceramics [18, 19], metals [20, 21] and carbon allotropes [22, 23]. Particle laden polymers (PLP) are widely used in polymer-based TIMs, such as thermal grease, PCMs and thermal pads. However, the filler particles are distributed randomly inside the polymer, which leaves a small chance for the particles to form a thermally conductive path for heat rejection. To increase the possibility to form heat paths, high filling ratio of particles are added to the polymer matrix as shown in Figure 1.2, but this leads to significant reduction of mechanical compliance. As an alternative way to create heat paths inside polymer, high aspect ratio fillers are aligned with the heat flow [24, 25], but the alignment process is complicated, and the thermal performance enhancement is not significant. Carbon nanotubes (CNTs) have extremely high axial thermal conductivities [26, 27], which are vertically aligned and bonded to surfaces to enhance contact thermal conductance [28, 29] as shown in Figure 1.3. Metal materials with high thermal conductivities are engineered to be compliant structures, like springs [30, 31] and wires [32, 33], and soldered to surfaces to achieve conformal contact and therefore enhance contact thermal conductance.

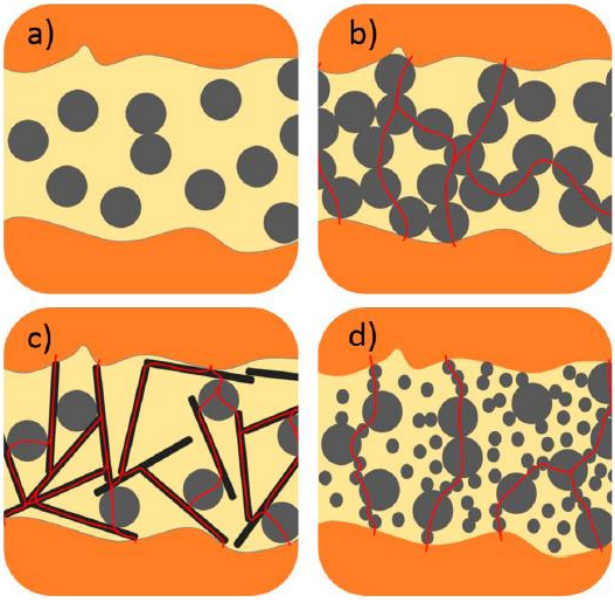

Figure 1.2. Illustration of percolation concepts in PLPs. (a) PLP with filler fraction below the percolation threshold. (b) PLP with filler fraction above percolation threshold, allowing thermally conductive pathways to form. (c) Combination of fillers with high aspect ratio can achieve percolation at lower filler fractions. (d) Combination of fillers with different sizes can achieve percolation at lower filler fractions. [9]

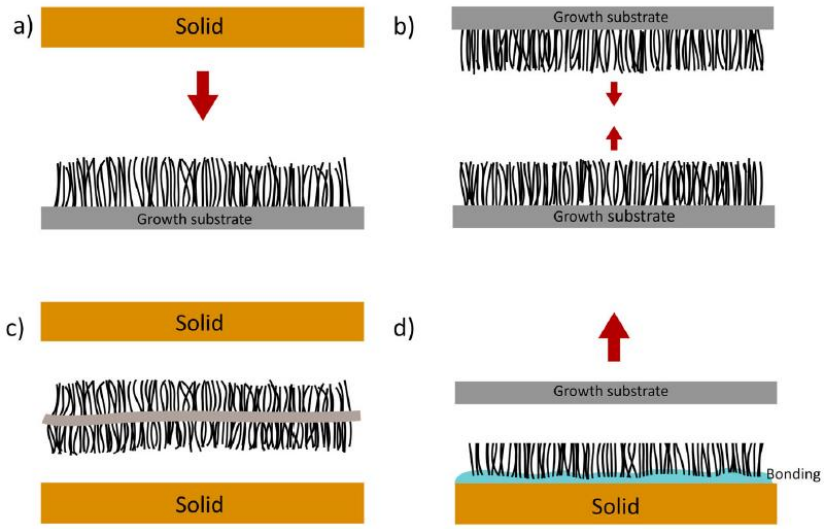

Figure 1.3. CNT array interface structures. (a) An example of one-sided interface. (b) An example of two-sided interface. (c) An example of CNT-coated foil interface. (d) Bonding of CNT arrays to another substrate using metal or chemical bonding. [9]

1.5 Challenges of TIM Design in Pluggable Applications

The extreme scaling of electronic and optoelectronic devices has led to a dramatic increase in their operating power density, resulting in ongoing thermal management challenges. In particular, parasitic contact resistances across solid–solid interfaces are ubiquitous in electronics packages and can contribute significantly to the overall thermal resistance to heat rejection. The design of thermal interface materials (TIM) has become increasingly critical to maintain device temperatures within appropriate performance and reliability limits through an enhancement in the thermal contact conductance across interfaces. This contact thermal resistance is mainly caused by micro-scale surface asperities (roughness) and wavy profile of surface (nonflatness) which severely reduce the contact area available for heat rejection.

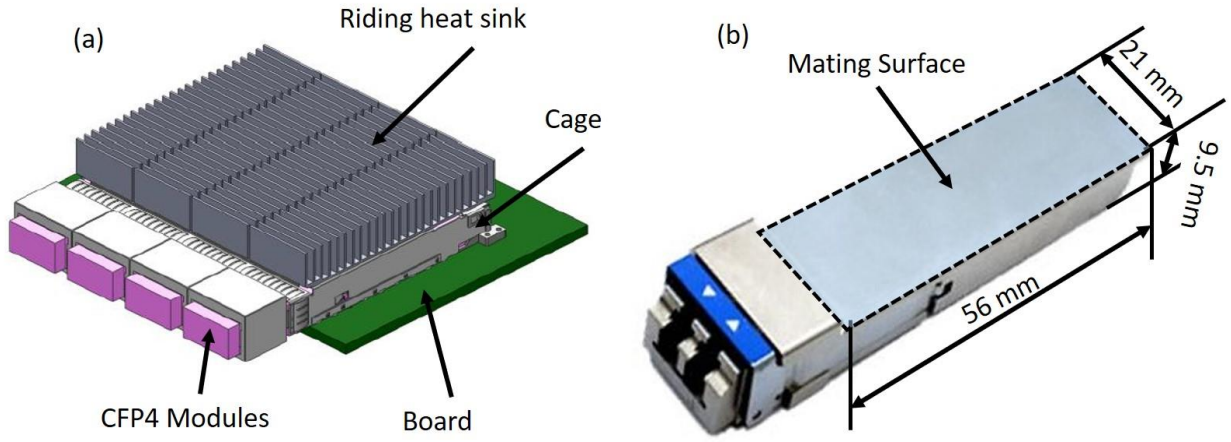

Figure 1.4. (a) Illustration of a working unit consisting of 4 CFP4 modules inserted into the host cage system. (b) An image of a commercially available CFP4 module with overall dimensions labeled. [35]

Some electronic applications, such as pluggable optoelectrical transceiver modules [34], require the heat generation device to repeatedly slide into and out of contact with the riding heat sink. A representative sliding application, CFP4 module [35], is shown in Figure 1.4. The CFP4 module is a kind of commercially available C form-factor pluggable (CFP) optoelectronic transceiver which is developed for the transmission of digital signals mainly for 100 Gigabit Ethernet systems. Typically, 4 CFP4 modules slide into the cage and contact the riding heat sink, which forms a working unit as shown in Figure 1.4 (a). A total power of 1.5–9 W needs to be

dissipated through a 56 mm × 21 mm surface with surface nonflatness of 10s μm and surface roughness of ~1 μm as shown in Figure 1.4 (b). A low working pressure of < 10s kPa is needed for sliding. Trivial surface polishing cannot remove the surface nonflatness.

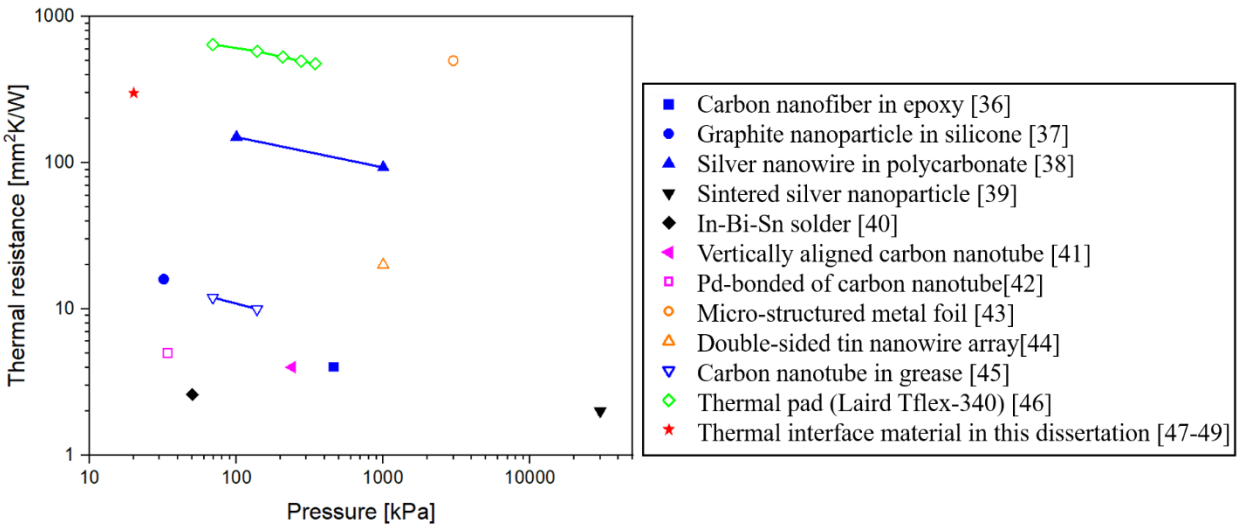

Figure 1.5. The plot of thermal resistance versus pressure for recent results and products [36-46] of thermal interface materials. The results are divided into three categories: particle laden polymers (blue), continuous metal phase TIMs (black), carbon nanotube array TIMs (magenta), mechanically compliant metal TIMs (orange), polymer nanowire array (purple) and commercial TIM references (green). The thermal interface material shown in this dissertation [47-49] is the red star.

Figure 1.5 shows thermal resistances for some recent results and products [36-46] of thermal interface materials. High pressures and permanent bonding, such as thermal adhesives [36, 37], sintered metal [39] and soldering [40], are disallowed due to the sliding requirement. Solid PLPs [36] do not work for this application; due to the random distribution of thermally conductive particles, high filling ratio of fillers are required which increase the stiffness dramatically, as described previously. The TIMs are expected to work for several times of sliding; structures which deform once plasticly [43, 44] are also discouraged. Wet materials, such as greases [45], can be squeezed out during sliding, which are discouraged. For thermal pads [46], typical compressive pressure at least 100s kPa is required to functionalize them as TIM, which exceed the working pressures of the pluggable optical module.

1.6 Structure of This Dissertation

The dissertation focuses on a kind of novel TIMs consists of engineered metallized polymer micro-spring arrays which works for pluggable applications. The polymer scaffold of the TIM is fabricated by using a custom projection micro-stereolithography (μSL) system. Metallization and surface polishing are applied on the polymer scaffold to enhance thermal conductivity for nonflat surfaces, while polymer coating is applied to metallized TIM for rough surfaces. Experimental setups are established to characterize thermomechanical properties and reliability of the TIM. A thermal demonstration on a commercially available pluggable application is conducted to check the overall thermal performance of the TIM. To further enhance the mechanical compliance of the micro-structured TIM, a new type of zero stiffness structure made up with double curved beams is designed. The double curved beam consists of a positive stiffness beam and a negative stiffness beam. A fabrication procedure is designed to build residual stresses in the structure, which leads to negative stiffness, and realized in the μSL system. Compression tests experimentally confirm the zero stiffness of the structure.

This report is separated into 6 chapters. Beside the introduction chapters, information of other chapters is listed below:

- Chapter 2 focuses on the fabrication and thermomechanical performance characterization of the TIM with zig zag micro-springs.
- Chapter 3 focuses on the design and numerical analysis of the TIM with hexagonal zig zag micro-springs.
- Chapter 4 focuses on the design and enhanced thermal performance of TIM with finned zig zag micro-springs.
- Chapter 5 focuses on the design, fabrication and demonstration of a near zero-stiffness material made of double curved beams built with residual stresses.
- Chapter 6 summarizes and concluded the dissertation.

2. TIM WITH ZIG ZAG MICRO-SPRINGS

2.1 Introduction

In this chapter, a new kind of metallized microstructured dry TIM is introduced to join nonflat surfaces (*e.g.*, 5 μm nonflatness) at low (10s-100s kPa) interfacial contact pressure by combining the cost-effective techniques of projection μSL and electroplating. Projection μSL is used to created 3D polymer scaffolds; electrodeposition is used to conformally coat the polymer scaffolds with a continuous layer of thermally conductive metal using a solution-based process. The final structure is an array of spring-like metallized microstructures which provide both high mechanical compliance and a continuous pathway for heat flow. Mechanical compliance of this microstructured dry TIM is characterized by measuring the deformation as a function of contact pressure. Compared to bare metal contact, thermal measurements are performed to demonstrate the consistency of thermal resistance yielded by this microstructured TIM under dry contact between polished metal surfaces with different nonflatness.

Significant portions of this chapter have been published in "Cui, J., Wang, J., Zhong, Y., Pan, L., & Weibel, J. A. (2018). Metallized compliant 3D microstructures for dry contact thermal conductance enhancement. *Journal of Micromechanics and Microengineering*, 28(5), 055005."

2.2 Methods

2.2.1 Structure Design

Figure 2.1 (a) shows a micro-structured TIM consisting of an array of zig zag micro-spring. Since the surface roughness can be trivially removed by polishing, this micro-spring is mainly designed to be compliant to accommodate surface nonflatness under low pressures. As shown in Figure 2.1 (a), the zig zag spring has the shape of the plate spring with overall height of 250 μm. The top surface is extended to achieve more contact area. The sharp corner of the spring is blend out and fortified to avoid the possible fraction under compression. 15 × 16 zig zag springs form an array with a pitch of 500 μm between two neighboring springs in both directions. Three solid ribs are embedded within the array, which are 50 μm shorter than the micro-springs, to protect the micro-springs from over-compression when the spring array is subjected to high contact pressures

over the working limit. A 500-μm-thick solid base layer is designed underneath the micro-springs for the convenience of handling and transfer. The footprint area of the whole TIM is 6 mm × 10 mm. As shown in Figure 2.1 (b), the zig zag micro-springs can be easily deformed and conform to a nonflat surface under low pressures so that the interfacial contact area is significantly increased compared to bare solid-to-solid contact. The whole surface of the polymer TIM is metallized to enhance its thermal conductivity.

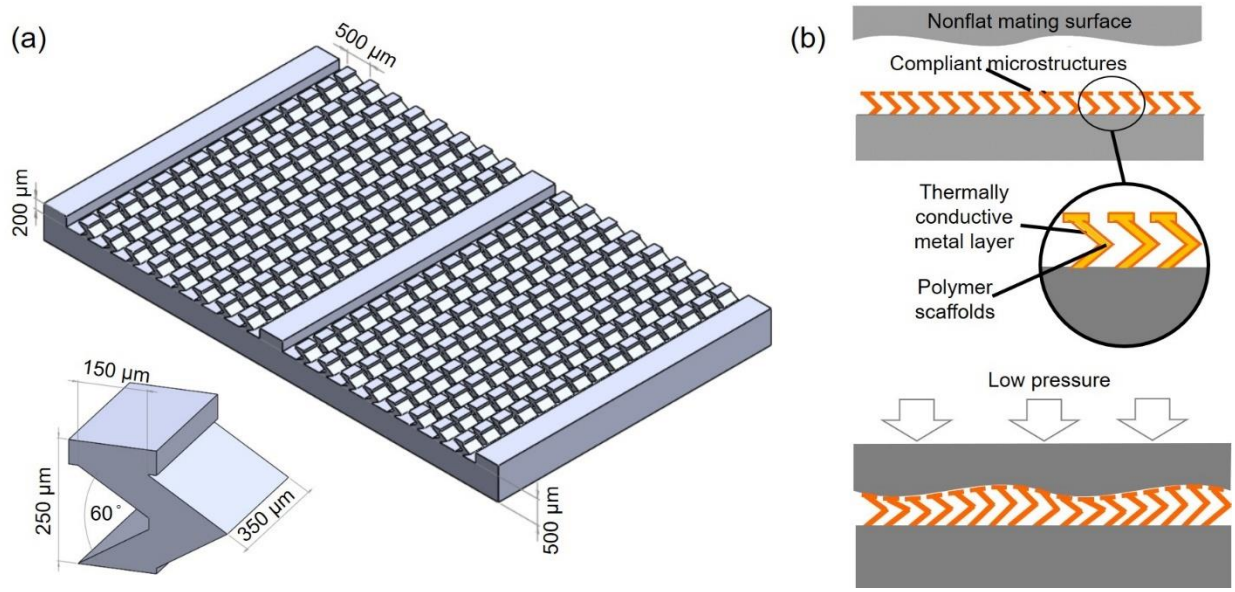

Figure 2.1. (a) Three-dimensional (3D) drawings of the microstructured thermal interface material (TIM) consisting of a zig zag micro-spring array (with inset dimensioned drawing of an individual zig zag spring element) and (b) schematic illustration of the mechanism by which a compliant microstructured TIM conforms to a nonflat surface [47].

2.2.2 Fabrication of polymer scaffolds

Micro-scale devices can provide solutions in some demanding applications in the fields of energy, security, food and medicines. Researchers have developed new methods for fabricating geometrically and structurally well-defined 3D geometries at small scales, including additive and subtractive processes [51-55]. However, there is lack of production and efficiency in some of the manufacturing processes to produce micro-structures.

The polymer scaffold of the TIM is built by using projection micro-stereolithography (μSL) technique. μSL has been used in fabrication of three-dimensional (3D) microscale structures in applications including biomaterial, photonic, energy storage and metamaterials [56-61]. Projection μSL is able to additively build 3D structures layer-by-layer with a high resolution down to several micrometers [56, 60, 61], and as low as even 0.6 μm [62].

This μSL fabrication process is cost-effective, benefiting from mature projection lithography technology and inexpensive photo-curable resin. An advantage of this approach is the ability to polymerize entire layers of resin at a time, which provides faster build speeds and less stitching error in comparison with other 3D microfabrication technologies that use point-wise scanning schemes, such as two-photon stereolithography [63, 64].

A custom projection μSL fabrication system is established to fabricate polymer scaffold, illustrated in Figure 2.2 (a). Before fabrication, a 3D model of the TIM structure is prepared and sliced every 10 μm in the height direction, which generates a series of two-dimensional (2D) cross section images. Several drops of liquid resin are trapped between a glass window and a substrate silicon wafer. UV light (wavelength 405 nm) from a LED lamp irradiates on a programmable digital micromirror device (DMD), which displays the 2D cross section images of current layer; then, the light is reflected to the top surface of resin and cure it. After that, UV light is switched off, and the substrate moves down 10 μm to let the fresh liquid resin into the fabrication area for next layer. The dynamic mask changes the image to the next layer. By repeating the previous steps, the 3D structure is fabricated layer-by-layer to form a 3D polymer scaffold for the TIM.

The projection μSL system is compatible with many kinds of photo-curable resins. In this work, we use a polyethylene glycol diacrylate (PEGDA) resin which is mixed with 0.5 wt% photoinitiator (Irgacure 918) and 0.2 wt% photoabsorber (Sudan I). When the UV light luminates on the resin, the photoinitiator first is activated and generates radicals which can trigger the polymerization of PEGDA. The photoabsorber is applied to control the depth that UV light can penetrate in the liquid resin. To develop an etching-free process for metallization, a kind of 1 wt% sensitization solution (tin (II) chloride water solution at 10 wt%) is mixed with the resin as the sensitization agent.

A 2-mm-tall Eiffel Tower structure is fabricated to confirm the function of the projection μSL system, as shown in Figure 2.2 (b). The horizontal lines on the sidewalls of the structure indicate the layer thickness of 10 μm. The grid pattern observed from the inset corresponds to the

pixels of DMD. The size of tower peak is <10 μm, which indicates the fabrication resolution of this system.

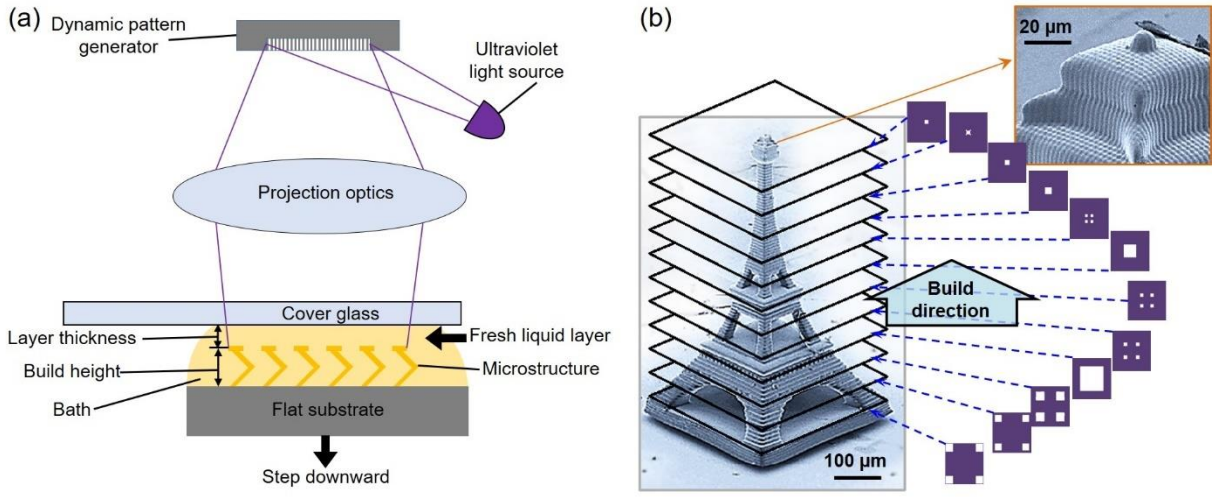

Figure 2.2. (a) Schematic diagram of the projection micro-stereolithography (μSL) system which uses UV light to solidify the photo-curable resin and build 3D structures. (b) Scanning electron microscope (SEM) image of a 2-mm-tall Eiffel Tower fabricated by stacking 2D images cross section layer-by-layer. The inset is a magnified image of the top of the structure. [47]

2.2.3 Metallization

The polymer microsprings are metallized in two sequential steps: nickel electroless plating [65, 66] and copper electroplating. For the nickel electroless plating, the polymer sample is first etched in a 0.25 wt% potassium permanganate (KMnO4, Sigma-Aldrich) aqueous solution at 80 °C to form small holes on the surface for anchoring of the metal layer. The structure is then sensitized in a 1 wt% tin (II) chloride ($SnCl_2$, Sigma-Aldrich) solution and activated in a 0.025 wt% palladium chloride ($PdCl_2$, Sigma-Aldrich) solution. The $PdCl_2$ reacts with $SnCl_2$ to generate small palladium particles on the surface that serve as a catalyst. Finally, the plating solution is 3 wt% nickel sulfate (NiSO4, Sigma-Aldrich) solution with 2 wt% sodium hypophosphite (NaH_2PO_2, Sigma-Aldrich) solution as a reducing agent, 1.7 wt% sodium malate ($C_4H_4O_5Na_2$, Sigma-Aldrich) solution as complexing agent, and 0.9 wt% acetic acid to adjust the pH value to 4-5. The coated nickel layer serves as an electrically conductive based material for the subsequent copper electroplating.

2.2.4 Characterization of Mechanical Compliance

An experimental setup is established to characterize mechanical compliance of the TIM under normal compression as shown in Figure 2.3. During the test, the TIM is set between two rigid surfaces which average the compressive force to the whole area. The sandwich of rigid surfaces and TIM is set on a three-axis translation stage. Weights are added on the loading platform and generate compressive pressures through the axial shaft passing through a linear bearing. A load cell (Omega LCFD-1kg; ± 0.015 N) is fixed at the end of the shaft to characterize the compressive force. A ball bearing is fixed under the load cell to make sure the force direction is always normal to the sample plate. A spring is used to balance the dead load of the loading platform, shaft and load cell. The deformation of the TIM is viewed and recorded by a digital camera through a high magnification zoom lens. The mechanical compliance is achieved by successively increasing the loading and recording the deformation.

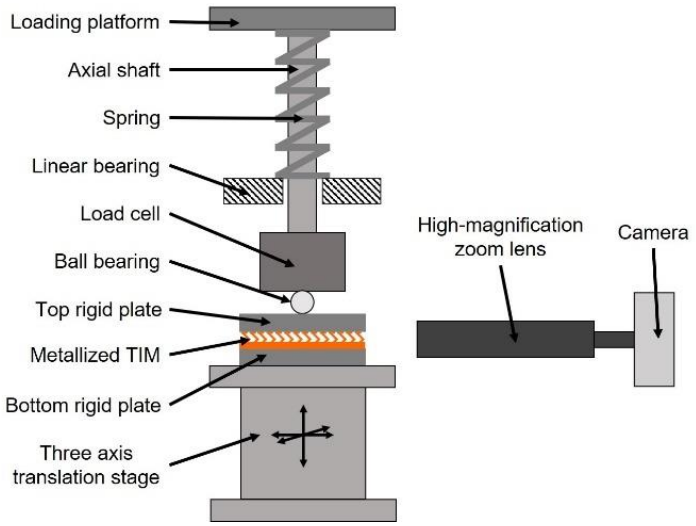

Figure 2.3. Schematic diagram of the experimental setup to characterize the mechanical compliance of the TIM [47]

2.2.5 Characterization of Thermal Resistance

A test facility is set up to measure contact thermal resistance as shown in Figure 2.4 (a). There are two aluminum (6061, thermal conductivity 150 $W \cdot K^{-1} \cdot m^{-1}$) bars serving as the thermal conduction path. The bars have the same cross section area with the TIMs inserted in between. A

resistance heater is used as the heat source attached on the top, and a pin fin heat sink is attached at the bottom to remove heat. Thermal insulation (PEEK, thermal conductivity ~0.3 $W \cdot m^{-1} \cdot K^{-1}$) is applied around the whole setup to keep heat conduction in one direction. Five thermocouples (Omega T-type, ±0.2℃) are set in different preset position on bars to measure the temperatures along the center line of the setup. After achieving steady state, heat flux and bottom temperature are exacted from the temperature gradient measured from the four thermocouples in the lower bar, and the top temperature is achieved from the thermocouple in the upper bar. The facility is designed to measure the total insertion thermal resistance (R_{tot}) between the bars as shown in Figure 2.4 (b). The effective thermal resistance (R_{eff}) of TIM is defined including resistance of micro-springs (R_s) and interfacial resistance between micro-springs and mating surface ($R_{c,top}$), which indicates an ideal case that the micro-springs are directly bonded to the working surface. The TIMs have a base layer which introduces resistance of base layer (R_b) and interfacial resistance between substrate and contact surface ($R_{c,bot}$) to R_{tot}.

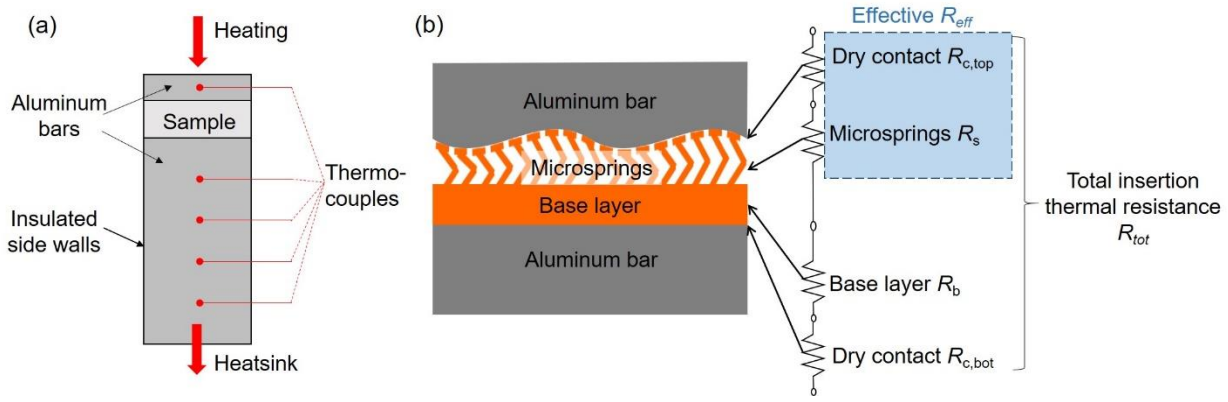

Figure 2.4. (a) Schematic diagram of the experimental setup to characterize total insertion thermal resistances of TIMs. (b) Illustration of the component resistances contributing to the total insertion thermal resistance measured in the test facility. [47]

2.3 Results

2.3.1 Polymer and Metallized TIMs

The images of the TIM made of basic zig zag springs before and after metallization are shown in Figure 2.5. All of the 240 zig zag micro-springs, as shown in Figure 2.5 (a), are fabricated to the same dimensions without significant defects, which shows a good fabrication uniformity across the whole fabrication area. The cross section of the metallized TIM is observed under a high-magnification microscope to examine the thickness of metal layer. After electroless nickel plating as shown in Figure 2.5 (b), the nickel-coated micro-springs have shiny, smooth and almost uniform layer of ~0.5-μm-thick nickel (thermal conductivity ~50 $W \cdot m^{-1} \cdot K^{-1}$). After the electroplating, as shown in Figure 2.5 (c), the nickel-coated micro-springs are coated with thermally conductive copper (thermal conductivity ~400 $W \cdot m^{-1} \cdot K^{-1}$) of ~10 μm thick. The microscopic and scanning electron microscopy (SEM) pictures of the copper-coated micro-springs are shown in Figure 2.5 (d, e). The copper layer is almost uniform in thickness, but the surface roughness of copper coating is relatively high.

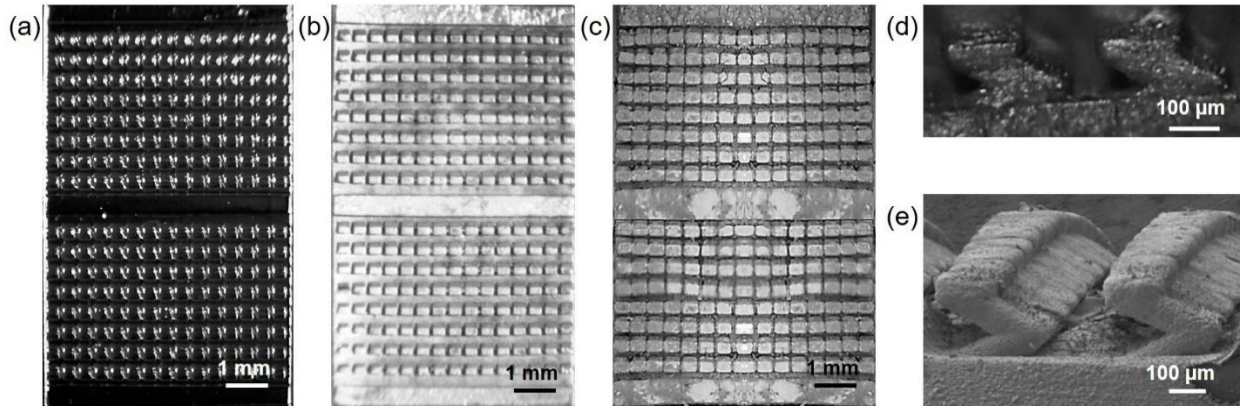

Figure 2.5. (a, b, c, d) Microscopic images of top view of (a) polymer, (b) nickel coated and (c) copper coated TIM made of zig zag springs, and (d) side view of copper coated zig zag micro-springs. (e) Scanning electron microscopic (SEM) image of copper coated zig zag micro-springs. [47]

2.3.2 Mechanical Compliance

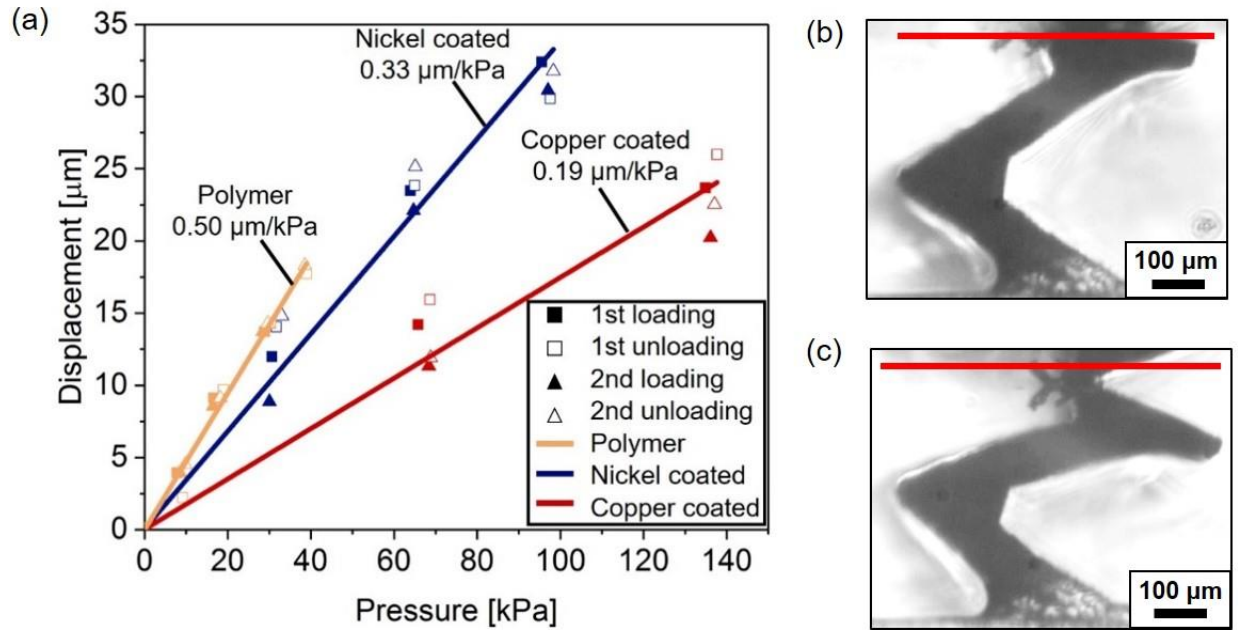

Figure 2.6. (a) Characterization of the displacement as a function of the applied pressure of the polymer, nickel-coated, and copper-coated TIMs with zig zag micro-springs: The solid symbols indicate loading direction and open symbols unloading; squares indicate the first loading cycle and triangles the second cycle. Solid lines are the linear fits of the data. The slopes of best linear fit solid lines indicate mechanical compliance of the TIMs. Microscopic images of the side view of a single polymer zig zag micro-spring (b) without and (c) with compression. [47]

To evaluate the influence of metal coating to the mechanical compliance of TIM, the mechanical compliance of the TIM consisting of zig zag springs with three different coatings: no coating (polymer), nickel coating and copper coating. We load the structures up to ~40-140 kPa. Figure 2.6 (a) shows the vertical displacement of the zig zag springs as a function of the applied pressure for two loading and unloading cycles each. The deformation of the structures is linear, elastic, and has no hysteresis over this range of applied pressure. The displacement and pressure show good linearity; the mechanical compliance can therefore be extracted from the data using a linear fit. The compliances of polymer, nickel-coated and copper-coated structures are 0.50, 0.33, 0.19 μm/kPa respectively. The compliance of the TIMs decreases with the increase of metal layer thickness, but still more than three orders of magnitudes better than that of pure metal micro-springs having the same geometry predicted by a simplified beam-bending model. Under

compression, the top surface of the zig zag micro-spring lose contact with the mating surface due to the asymmetric bending of the whole structure, as shown in Figure 2.6 (b, c). This tip deflection increases contact thermal resistance between the TIM and mating surface, which is solved in the next designs of hexagonal and finned zig zag springs.

2.3.3 Thermal Resistances for Flat Surface

To understand the effect of metallization, the thermal resistances of TIMs with zig zag micro-springs with different coatings: polymer scaffold, nickel-coated and copper-coated, are evaluated for a flat and polished mating surface under the same pressure (~300 kPa). At this high pressure, the curvature in the base layer, caused by residual stress after metallization, can be flattened; the micro-springs are in a maximally compressed state down to the protective ribs. The micro-springs have no visible deformation and can recover to the original shape and dimension after being compressed under the pressure of ~300 kPa. As shown in Figure 2.7 (a), the mating surface is generally flat and smooth but has some deep scratches which is not removed by hand polishing. As shown in Figure 2.7 (b), the polymer TIM have the highest total thermal resistance of 8100 $mm^2 \cdot K/W$. Due to the addition of the high-thermal-conductivity metal layers, the nickel- and copper-coated TIMs have lower resistances of 4200 and 2800 $mm^2 \cdot K/W$, respectively.

The effective thermal resistances are obtained by subtracting base layer resistance R_b and bottom contact resistance $R_{c,bot}$ from the total insertion resistances. Measurement of total insertion thermal resistances R_{tot} of solid polymer blocks with different thickness is conducted under same pressure of ~300 kPa to characterize R_b and $R_{c,bot}$. R_b increases linearly with the thickness of the blocks, while $R_{c,bot}$ does not change due to the same interfacial condition and the same pressure. By plotting R_{tot} of blocks with their thickness, R_b and $R_{c,bot}$ can be obtained from the slope and intercept of the plot, which are 420 $mm^2 \cdot K/W$ and 1180 $mm^2 \cdot K/W$, respectively. The effective thermal resistances of the TIMs (R_{eff}) are 6530, 2630 and 1210 $mm^2 \cdot K/W$ for the three coating configurations of polymer, nickel-coated, and copper-coated TIMs, respectively. The effective thermal resistance (R_{eff}) is reduced by 80% after metallization with copper. To further decompose the components of the effective thermal resistance, the thermal resistances of the three TIMs (R_s), assuming simplified one-dimensional heat conduction through the micro-spring using known material properties, are calculated to be 5180, 1130, and 40 $mm^2 \cdot K/W$, respectively. The

remaining resistance is attributed to $R_{c,top}$, which are 1350, 1500, and 1170 $mm^2 \cdot K/W$, respectively. As expected, $R_{c,top}$ is similar for all three cases under the same contact pressure.

2.3.4 Effective Thermal Resistances for Nonflat Surface

Although the thermal resistance measurements for the flat mating surface allows understanding of the components of total insertion thermal resistances, the purpose of the TIM is to enhance the contact conductance for highly nonflat surfaces. To further evaluate the thermal resistance of the TIM mating with a nonflat surface, a process of laser etching is applied on the contact surface of the upper aluminum bar to create a surface with nonflatness of ~5 μm. As shown in Figure 2.7 (c), the surface profile is a series of periodic grooves of 2 mm wide and ~10 μm deep with 0.5-mm-wide plateaus in between. The surface is then polished to remove most of surface roughness. The effective thermal resistances of the copper-coated TIM are compared to contact thermal resistances of direct metal-to-metal interface for flat and nonflat surfaces, as shown in Figure 2.7 (d). Contact thermal resistances of direct metal-to-metal interface are 120 and 700 $mm^2 \cdot K/W$, for flat and nonflat mating surface respectively. The thermal resistances increase by ~5 times due to the reduction of contact area. Effective thermal resistances of TIM are 1210 and 1280 $mm^2 \cdot K/W$, for flat and nonflat mating surface respectively. The effective thermal resistances increase by ~6%, which means the TIM performs similarly for different surface nonflatness as long as the compress pressure is large enough to deform it to conformally contact the surface. This result provides a critical proof of concept that the dry contact thermal resistance of this compliant TIM with zig zag micro-springs is nearly unaffected by the presence of surface nonflatness.

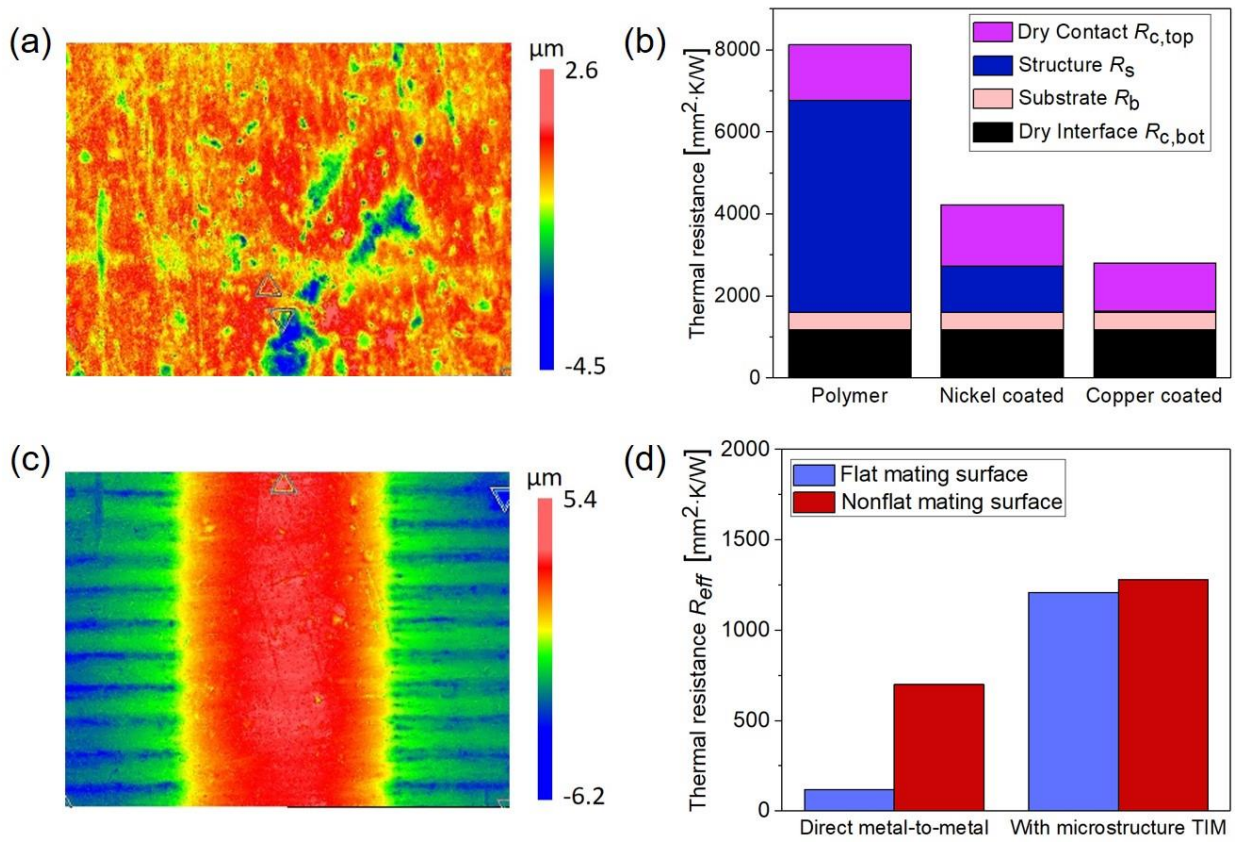

Figure 2.7. Surface profiles of the (a) flat and (c) nonflat mating surfaces over an area of 1.4 mm × 1 mm characterized by an optical interferometer. (b) Thermal resistances of the TIM having polymer, nickel-coated, and copper-coated zig zag micro-springs for flat mating interface. (d) Comparison of effective thermal resistances for flat and non-flat mating interfaces with the copper-coated TIM and without (i.e., direct metal-to-metal). [47]

3. TIM WITH HEXAGONAL ZIG ZAG MICRO-SPRINGS

3.1 Introduction

In the last chapter, a zig zag spring is introduced as TIM for pluggable applications. However, the zig zag geometry can potentially lose some contact area when compressed, which causes an increase in the contact thermal resistance between the structure and the mating surface. This loss of contact area comes from the asymmetric geometry of the zig zag spring; when compressed, the tip of the spring tilts and lifts away from the mating surface.

A newly designed hexagon spring structure is introduced in this chapter to solve the problems. This hexagon spring geometry is centrosymmetric, which keeps the top surface of the spring in contact with the mating surface when compressed. The mechanical compliance of the polymer hexagon spring under compression is predicted by a simulation and then confirmed by using a custom-made mechanical compliance tester. Compared to the zig zag spring geometry, the hexagon spring remains in complete contact with the mating surface under compression. After metallization, the thermal conductance of the hexagon spring is dramatically enhanced. Thermal resistance measurements confirm the metallized hexagon springs performs consistently for mating surfaces with increasing nonflatness, indicating that the springs conform to the opposing surface. This is compared to a dramatic change in the thermal resistance for metal-to-metal contact when nonflatness is introduced without the springs in place.

Significant portions of this chapter has been published in "Cui, J., Weibel, J. A., & Pan, L. (2018). Metallized Three-Dimensional Centrosymmetric Microstructures to Enhance Dry Contact Thermal Conductance across Nonflat Interfaces. *The 16th International Heat Transfer Conference (IHTC)*, IHTC16-23666."

3.2 Methods

3.2.1 Structure Design

The zig zag spring undergoes tip deflection and lose contact with the mating surface under compression which dramatically decreases the interfacial contact area, as shown in Figure 2.6 (b, c). This tip deflection comes from the asymmetric geometry of the zig zag spring. To solve this

problem, a hexagonal zig zag spring is developed which consists of six centrosymmetrically arranged zig zag springs, as shown in Figure 3.1 (a). Compared to the asymmetric geometry of zig zag spring, the centrosymmetric geometry enables hexagonal spring to keep conformal contact with the mating surfaces under compression. When the hexagonal spring is compressed, the rotation of the top surface may cause friction between the top surface and mating surface and damage to the spring. The zig zag shape, instead of tilted structs, makes the lower half and upper half of the hexagonal spring rotate reversely, which leads to no rotation of the top surface under compression. The height of the hexagonal spring is 350 μm and each of the six zig zag springs has a square cross section of 100 μm × 100 μm. As shown in Figure 3.1 (b), the micro-structured TIM consists an array of 9×12 hexagon springs with pitches of 720 μm and a 400-μm-thick base layer. The TIM has a footprint area of 10 mm × 6 mm.

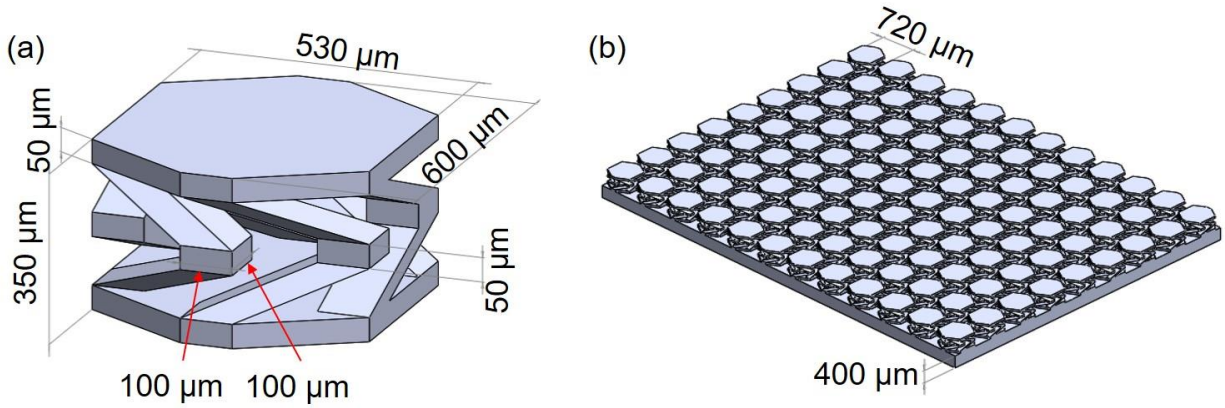

Figure 3.1. 3D drawings of (a) the hexagon zig zag micro-spring and (b) the TIM which consists of an array of hexagonal springs. Critical dimensions are labeled. [48]

3.2.2 Simulation Approach

To compare the mechanical performances of the hexagonal and zig zag spring under compression, finite element numerical (FEM) simulations are conducted in SOLIDWORKS Simulation. The Young's modulus of the material, cured polymer described in Section 2.2.2, is set to be 17 MPa and the Poisson's ratio set to be 0.3, which are achieved by compressing a sample with an array of pillars made of the same material. The bottom surfaces of the springs are fixed

and a uniform pressure of 10 kPa is applied onto the top surfaces. All the other surfaces are set to be stress free. Meshes of the structure are also generated in SOLIDWORKS Simulation, which uses a curvature-based meshing scheme with a maximum element size of 35 μm. An iterative solver, FFEPlus, is used in these simulations.

3.2.3 Experimental Approach

The TIM with hexagonal zig zag micro-springs is fabricated and metallized in the same way as the zig zag micro-springs, as described in Section 2.2.2 and Section 2.2.3.

3.3 Results

3.3.1 Simulation Results

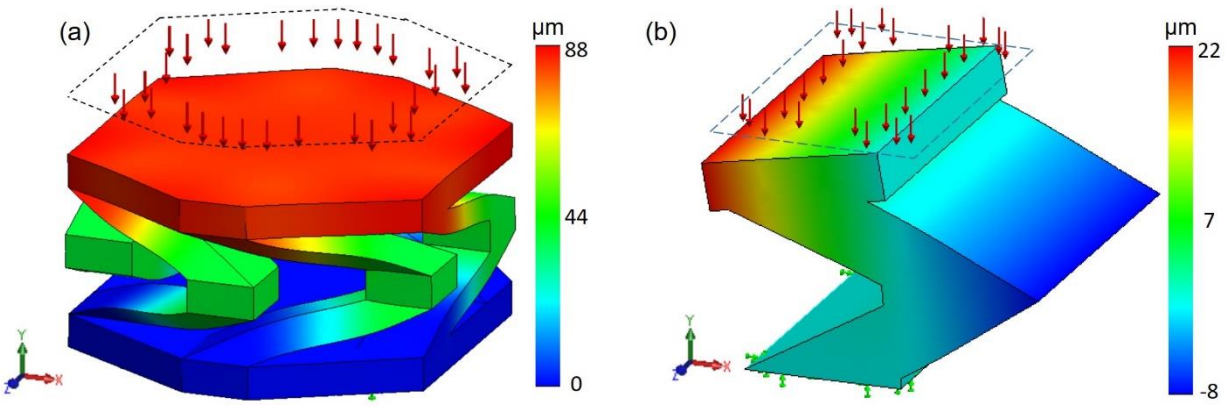

Figure 3.2. The vertical displacements exaggerated deformation of polymer (a) hexagon spring and (b) zig zag spring under a normal of 10 kPa. The dash lines indicate the original position of the top surfaces of the springs. The uniform color of the top surface of hexagonal spring indicates its uniform contact with the mating surface under compression.

The simulated vertical (along y-axis) displacements and exaggerated deformation of an individual polymer hexagonal spring and zig zag spring under a normal pressure of 10 kPa are shown in Figure 3.2. Positive displacements indicate that the springs move downward (-y direction) locally at these positions under compression, while the negative displacements indicate upward (+y direction). As shown in Figure 3.2 (a), the top surface of the hexagonal spring has a nearly

uniform vertical displacement, which means that the top surface of the hexagon spring remains parallel to the bottom surface under compression. As shown in Figure 3.2 (b), the top surface the zig zag spring has different vertical displacements in different locations. The shape of the compressed zig zag spring shows that its tip is tilted to one side, which causes the spring to lose contact with the mating surface. An average vertical displacement of 85 μm is achieved at the top surface of the hexagon spring. The 10 kPa pressure is only applied to the hexagonal top surface of ~270,000 μm^2, while the hexagonal spring occupies a square footprint area of 720 μm × 720 μm in the array. The effective pressure is calculated to be 5.2 kPa. The simulation results show that the mechanical compliance of polymer hexagon spring array is 16.3 μm/kPa.

3.3.2 Fabrication

A microscopic top view image of the TIM with hexagonal spring made of semi-transparent polymer is shown in Figure 3.3 (a). All of the 108 hexagonal springs are fabricated to the same dimension without obvious defects. Top view images of the hexagonal spring array after nickel and copper coating are shown in Figure 3.3 (b) and (c) respectively. After electroless nickel plating, the nickel layer is shiny and has a uniform thickness of ~0.5 μm. After copper electroplating, the TIM is further coated with a ~10-μm-thick layer of copper. Figure 3.3 (d) shows a magnified image of the tilted side view of a single copper-coated hexagonal spring. The surface of the copper layer is visually rougher than the base nickel layer.

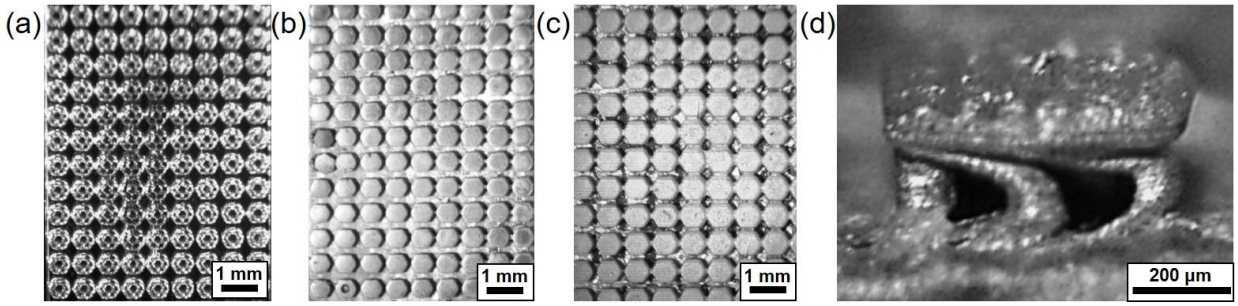

Figure 3.3. (a, b, c, d) Microscopic images of top view of (a) polymer, (b) nickel coated and (c) copper coated TIM made of hexagonal zig zag springs, and (d) tilted side view of a single copper coated hexagonal spring. [48]

3.3.3 Mechanical Performance of Polymer TIM under Compression

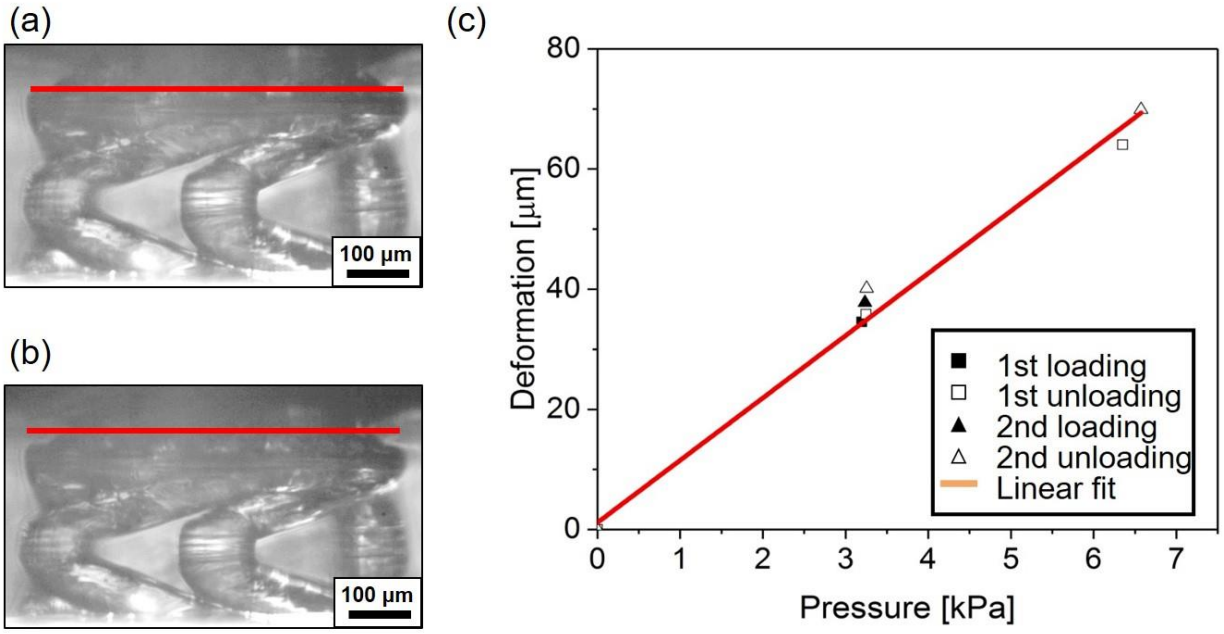

Figure 3.4. Microscopic images of the side view of a single polymer hexagonal zig zag micro-spring (a) without and (b) with compression. (a) Characterization of the displacement as a function of the applied pressure of the polymer, TIM with hexagonal micro-springs: The solid symbols indicate loading direction and open symbols unloading; squares indicate the first loading cycle and triangles the second cycle. Solid lines are the linear fits of the data. The slopes of best linear fit solid lines indicate mechanical compliance of the TIM. [48]

The mechanical performance of the polymer TIM with hexagonal zig zag micro-springs is characterized by using the experimental setup described in Section 2.2.4. Pressures of 0-7 kPa is applied to the polymer TIM, and The TIM is compressed to a maximum deformation of ~70 µm which is 20% of the spring height. During compression, unlike the tip deflection of zig zag spring shown in Figure 2.6 (b, c), the top surfaces of the springs remain in conformal contact with the mating surface as shown in Figure 3.4 (a, b). Figure 3.4 (c) plots the measured vertical deformation of the TIM as a function of the applied pressure. Two loading and unloading cycles are conducted to capture potential hysteresis and repeatability. The data have good linearity and no hysteresis, which shows that the TIM deforms elastically. The mechanical compliance is obtained from the slope of linear fitting of the data. The compliance of the polymer hexagon spring array is 10.5 µm/kPa, which shows reasonable agreement with the mechanical compliance predicted by

simulation (16.3 μm/kPa). This demonstrates that the TIM consisting of polymer micro-springs can be designed to achieve a target mechanical compliance after μSL fabrication.

3.3.4 Effective Thermal Resistances

Total insertion thermal resistances (R_{tot}) of the copper-coated TIM with hexagonal zig zag micro-springs for flat and nonflat surface is characterized under a low pressure of 20 kPa by using the experimental setup described in Section 2.2.5. Effective thermal resistances (R_{eff}) are separated from R_{tot} and by using the method described in Section 2.3.3. R_{eff}s of the TIM are compared to direct metal-to-metal contact under the same pressure. The profiles of mating flat and nonflat surfaces are shown in Figure 2.7 (a) and (c) in the previous section. Figure 3.5 shows the measured R_{eff} for the direct metal-to-metal contact and for the metallized spring array as a dry TIM. For the direct metal-to-metal contact, the thermal resistance increases from 350 $mm^2 \cdot K/W$ to 1830 $mm^2 \cdot K/W$ from the flat to nonflat mating surface. The resistance increase of over 4 times is mainly caused by reduction of contact area. For the copper-coated TIM, R_{eff} only increases by ~5%, from 1800 $mm^2 \cdot K/W$ to 1880 $m^2 \cdot K/W$. Although the direct metal-to-metal contact has a lower thermal resistance when the surface is flat, the R_{eff} of the copper-coated spring array is almost not affected by nonflatness of the mating surface and nearly equals direct contact resistance for the nonflat mating surface.

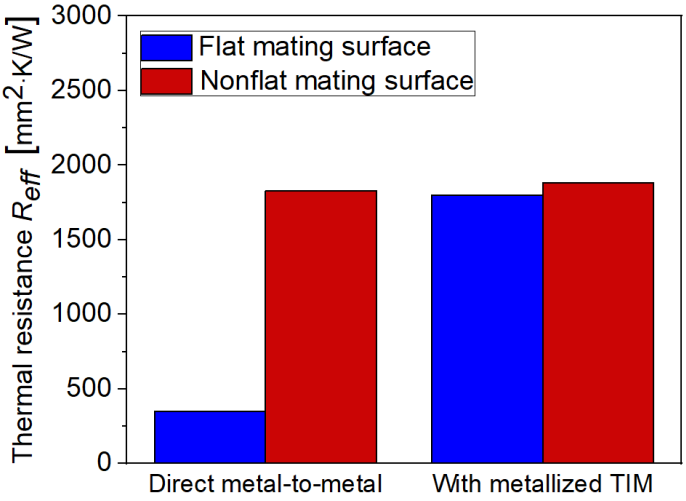

Figure 3.5. Effective thermal resistances for flat and nonflat mating surface with or without the copper-coated TIM with hexagonal zig zag springs array inserted

4. TIM WITH FINNED ZIG ZAG MICRO-SPRINGS

4.1 Introduction

In the previous two chapters, two kinds of micro-spring array are demonstrated to work as a TIM for pluggable applications. However, the thermal resistance of these TIMs are still not as good as commercial thermal pads. Besides, the polymer base designed under the micro-spring array can provide the advantages for handling as a standalone material or integration convenience, at the toll of an increased insertion resistance.

In this chapter, a new dry TIM made of metallized finned zig zag micro-springs that conforms to highly nonflat surfaces under low pressures, as required for pluggable thermal interface applications. The high mechanical compliance is structurally achieved by using the zig zag microscale springs that can easily deform under low pressures, with symmetric deformation to maintain in consistent contact with the mating surface. The high thermal conductance is achieved by metallizing the springs to form highly conductive thermal pathways. Microscale fins are added to the rigid portion of the spring structure, such that there is a significant increase in the surface area for metallization without reducing the compliance. A thin layer of soft polymer coating is applied on top of the metallized micro-springs, which is capable of conforming to surface nonflatness and microscale roughness, can reduce the thermal interface resistance between an optical module and a heat sink. This new dry TIM can be directly fabricated onto the device or heatsink surfaces to provide an enhanced interfacial conductance. We measure the insertion thermal resistance of this dry TIM and demonstrate that it provides significantly improved thermal conductance compared to that of metal-to-metal contact for nonflat interfaces under low pressures. A commercially available C form-factor pluggable (CFP) optoelectronic transceiver module having a surface nonflatness of 10s μm and a surface roughness of 0.5 μm is used for the demonstration. A thin layer of a soft polymer (polystyrene) is coated on the tops of metallized micro-springs to accommodate micro-roughness on the mating surface. The total insertion contact thermal resistance is measured when the dry TIM is placed between the surface of a CFP4 module and its riding heat sink under a compressive pressure of 20 kPa. Compared to the direct contact case, the contact thermal resistance is reduced by ~40% when the TIM is inserted. The short-term reliability is assessed by sliding the TIM across the mating surface of the optical module for 100

plug-in and plug-out cycles while under compression. There is no visible damage to the TIM or degradation in thermal performance after the cycles.

Significant portions of this chapter have been published in "Cui, J., Wang, J., Weibel, J. A., & Pan, L. (2019). A compliant microstructured thermal interface material for dry and pluggable interfaces. *International Journal of Heat and Mass Transfer*, 131, 1075–1082" and "Cui, J., Pan, L., & Weibel, J. A. (2019). Demonstration of a Compliant Micro-Spring Array as a Thermal Interface Material for Pluggable Optoelectronic Transceiver Modules. In *International Electronic Packaging Technical Conference and Exhibition* (Vol. 59322, p. V001T02A004). American Society of Mechanical Engineers".

4.2 Methods

4.2.1 Structure Design

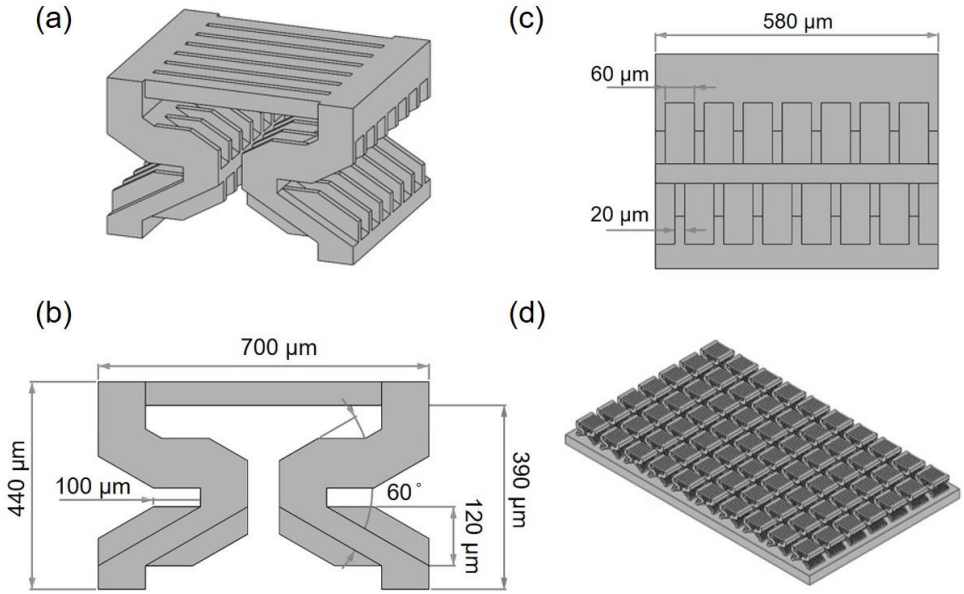

Figure 4.1 (a) Dimetric, (b) front, and (c) side views of the 3D model of an individual finned zig zag micro-spring. (d) Isometric view of 3D model of the TIM consisting of an array of finned zig zag micro-springs. [49]

A thermally conductive design of the finned zig zag spring is shown in Figure 4.1. The finned zig zag spring has a symmetric shape of two basic zig zag springs arranged back to back.

The top surfaces the two zig zag springs are connected with a top plate. The slots on the plate is used to avoid large, flat and smooth surface which is hard to metallize. 20-μm-thick fins are designed on the side walls of the springs, which create detours on the surface and increase the surface area for metallization to enhance thermal conductivity of the TIM. The height of the finned zig zag spring is 440 μm, and its footprint area is 700 μm × 580 μm. 7 × 10 finned springs form an array with a gap of 200 μm between two neighboring springs in both directions. The dimensions of the base layer are 10 mm (L) × 6 mm (W) × 0.2 mm (H).

On the other hand, a typical electronic package surface has both surface nonflatness and surface roughness. The micro-springs with lateral dimension of 100s μm are able to accommodate surface nonflatness with pitch of ~100s μm. However, surface roughness has a much smaller pitch of ~1 μm, which cannot be conformally accommodated by the micro-springs. Therefore, a hierarchical thin layer of polymer is coated on top of the metallized micro-springs to accommodate surface roughness as shown in Figure 4.2. The soft polymer layer can be easily deformed under low pressures and fill the void caused by surface roughness. Although the thermal conductivity of polymer is small, the small thickness limits its thermal resistance.

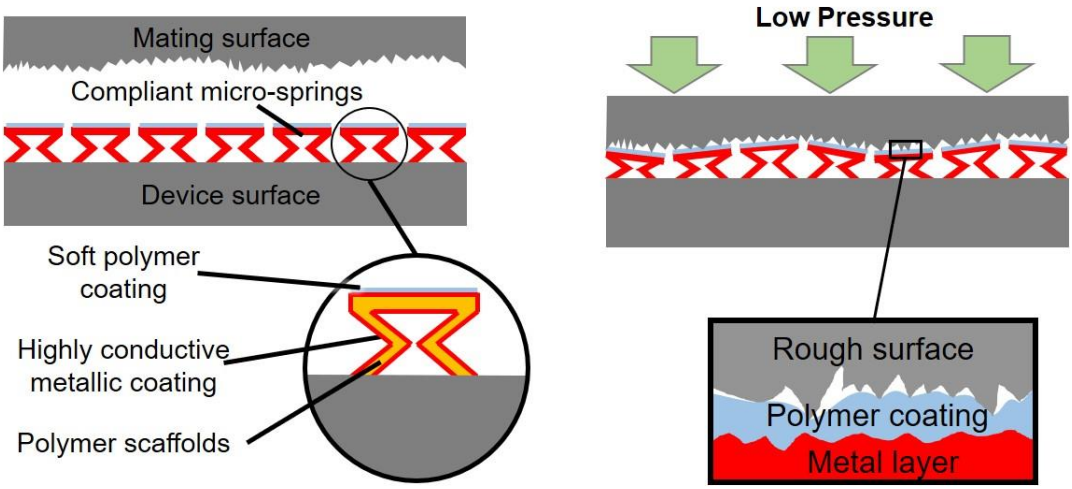

Figure 4.2. Working mechanism of the TIM made of compliant polymer-coated metallized micro-springs that conformally contacts with a nonflat and rough mating surface at a low pressure. The compliant micro-springs accommodate surface roughness, while the soft polymer coating accommodates surface nonflatness. [50]

4.2.2 Fabrication

The polymer scaffolds of the TIM with finned zig zag micro-springs are fabricated by using the projection μSL technique described in Section 2.2.2.

4.2.3 Metallization and Surface Polishing

The metallization process in Section 2.2.3 works well for zig zag and hexagonal micro-springs which have smallest feature size of ~100s μm. However, the chemical etching process damages the fin features (20 μm) in finned zig zag springs. To eliminate the chemical etching process, 1 wt% of the sensitization solution with high concentration (tin(II) chloride water solution at 10 wt%) is mixed with resin and buried inside the polymer scaffold during fabrication process. After soaking the polymer scaffold into the activation solution, sensitization agents buried in the scaffold react with activation agents, which generates palladium particles embedded on the surfaces as catalyst. The metallization reaction happens around the palladium particles and then spread to the whole surface. The palladium particles also work as anchors of the metal layer to the polymer scaffold. Besides, the copper electroplating process can generate relatively thick layer of copper, while the surface quality of the copper layer is poor. For finned zig zag spring, with the increased surface area, the thickness of copper is not necessarily thick to enhance thermal conductance, but the surface quality needs to be better to achieve lower contact thermal resistance. Therefore, electroless copper plating process [66] is applied to the finned zig zag spring, which can metallize surfaces with copper layer of high surface quality. The sensitization and activation process for the electroless copper plating is same as the electroless nickel plating. The electroless copper plating is conducted in a 60 ˚C bath of an aqueous solution of 0.45 wt% copper sulfate ($CuSO_4$) with 1 wt% formaldehyde (CH_2O) as a reducing agent and 2 wt% potassium sodium tartrate ($KNaC_4H_4O_6$) as a complexant. The pH value of the solution is adjusted to the range of ~9 to 10 by using 0.4 wt% sodium hydroxide (NaOH). The copper layer is easily oxidized in air, especially when moisture is exposed. To protect the copper layer, a thin layer of nickel is applied on the copper-coated TIM by using electroless nickel plating described in Section 2.2.3.

To remove some of the debris and asperities of the metal layer, a process of hand polishing is applied on the top of the metallized TIM. A microfiber cloth (typically for cleaning eyeglasses and lenses) and a standard paste-type polishing compound (BRASSO) are used for polishing. The

metallized TIM is first attached to a flat surface, and the cloth coated with polishing compound is used to gently wipe the top surfaces of the micro-springs.

4.2.4 Polymer Coating

The TIM can conformally contact a nonflat and smooth surface, but not a rough surface, because the feature size of the micro-spring (~100 μm) is similar to the length periodicity of the surface nonflatness, but much larger than that of surface roughness (~1 μm). When the micro-springs contact a rough surface, the 'spikes' of the microscale asperities contact on a stiff metallized solid plate, which causes a significant reduction of contact area. Therefore, a thin layer of soft solid polymer is coated on the metallized TIM to enhance the contact thermal conductance. The soft polymer can be deformed under low compressive pressures and fill the air gaps between the rough mating surface and the TIM. 0.5 wt% of polystyrene (PS, molecular weight ~300) grains are dissolved in chloroform ($CHCl_3$) by sonicating. The top surface of the metallized TIM is immersed in the PS solution and dried in a ventilation hood. Chloroform evaporates at room temperature of ~20℃, and the PS left forms a thin layer of solid polymer on top of the TIM.

4.2.5 Characterization of Thermomechanical Performances under Sliding Contact

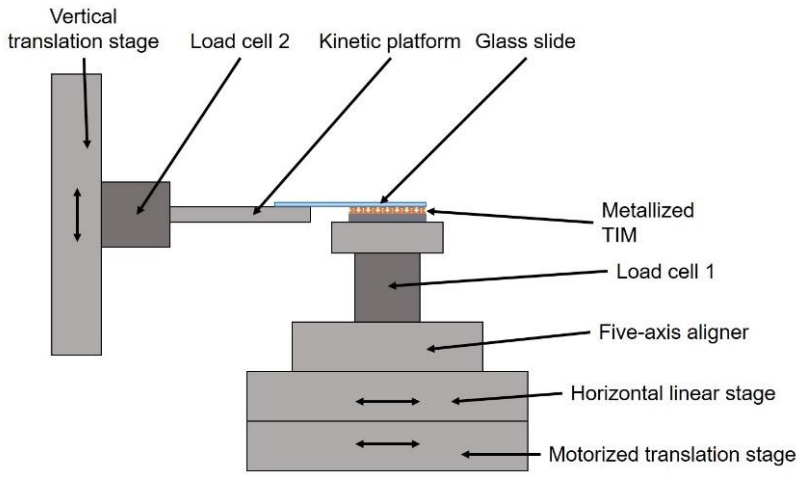

Figure 4.3. Schematic diagram of the experimental setup to observe and characterize the behavior of the TIM sliding against a glass slide. [49]

For pluggable applications, the TIM needs to slide into and out of contact with the device repeatedly. Therefore, an experimental setup is built to characterize the sliding contact behavior of the TIM, as shown in Figure 13b. During the test, the TIM is set on a plate to move against a glass slide. The glass slide is fixed on a kinetic platform; the TIM plate is fixed on a fix-axis aligner. The kinetic platform and the five-axis aligner work together to parallel the glass slide and the TIM. A horizontal linear stage and a motorized translation stage is used to control the position and motion of the TIM. The compressive pressure is applied by moving the vertical translation stage and measured by a load cell under the TIM plate (Load cell 1). The shear force is applied by moving the motorized translation stage and measured by a load cell fixed with the glass slide (Load cell 2). The top and side views of the TIM are observed through a zoom lens and a digital camera.

4.3 Results

4.3.1 Polymer and Metallized TIMs

Images of the TIM consisting of finned zig zag spring array at different process stages are shown in Figure 4.4. Figure 4.4 (a) shows a top view image of the polymer scaffold of the TIM. All the polymer micro-springs are fabricated properly and uniformly. Figure 4.4 (b) shows a top view image of the TIM after metallization. The metallized TIM has a uniform metal layer of ~2.5 μm, which is made of ~2 μm thick copper layer and ~0.5 μm thick nickel layer above the copper layer. A magnified image of top view of 4 micro-springs is shown in Figure 4.4 (c). The top surface of the metallized TIM is relatively rough, which have surface roughness of ~1 μm (achieved from surface profile characterized by an interferometer). After hand polishing, a top view of the metallized micro-springs is shown in Figure 4.4 (d) which has a reduced surface roughness of ~0.3μm. Figure 4.4 (f) and (g) show scanning electron microscopic (SEM) images of an individual metallized micro-spring after polishing. The fins are fabricated properly, and the thickness of the fins is ~20 μm, which approaches the fabrication resolution of the projection μSL system.

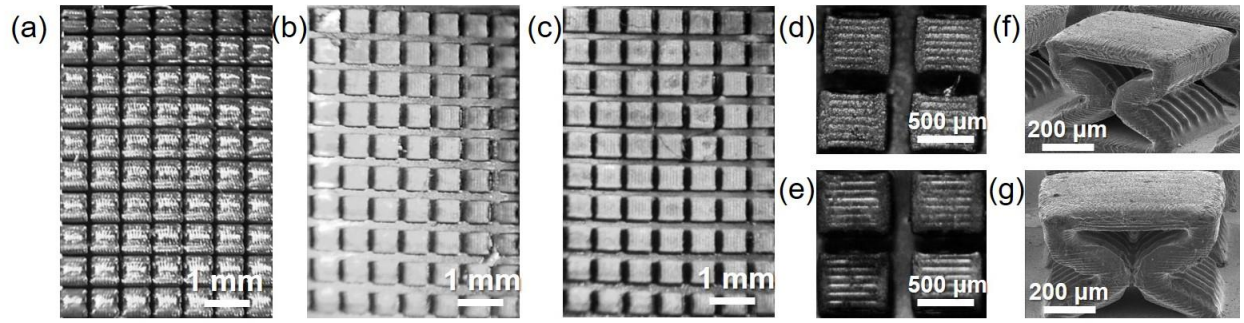

Figure 4.4. Microscopic images of the TIM with finned zig zag micro-springs at different fabrication stages: (a) top view of the polymer scaffold, top view of a metallized TIM (b) before and (c) after polishing and magnified top view of four micro-springs (d) before and (e) after polishing. SEM images of (f) dimetric and (g) front view of an individual metallized finned zig zag micro-spring after polishing. [49]

4.3.2 Young's Modulus and Thickness of Polymer Coating

The polymer (PS) coating is applied on the metallized and polished TIM. The Young's modulus of PS coating is characterized by nanoindentation to confirm its softness. Due to the high mechanical compliance of the micro-springs, the test is done on a polished nickel-coated copper plate with PS layer applied by using the same coating method. The Young's modulus is measured at different indentation depths at 25 different locations. The average Young's modulus is ~0.055 GPa at depth of 0.2 μm, which is ~3 order of magnitude lower than copper and nickel. When the depth increases to ~0.5 μm, Young's modulus increases dramatically, which indicates the thickness of polymer layer.

4.3.3 Effective Thermal Resistances for Flat and Polished Surfaces

To evaluate the effects of metallization and surface polishing, the effective thermal resistances of TIMs with finned zig zag micro-springs at different process steps: polymer scaffold, after metallization and after surface polishing, are evaluated under the same pressure (~20 kPa), by using the setup and method in Section 2.2.5 and 2.3.3. The mating surface is the flat surface shown in Figure 2.7 (a). As shown in Figure 4.5 (a), the polymer scaffold has the highest R_{eff} (3080 ± 120 $mm^2 \cdot K/W$) among all three kinds of TIMs. After metallization, R_{eff} is obviously decreased to 600 ± 50 $mm^2 \cdot K/W$, and after surface polishing, R_{eff} is further decreased to 280 ± 40 $mm^2 \cdot K/W$.

Metallization and surface polishing significantly decrease the effective thermal resistance of the TIM.

4.3.4 Effective Thermal Resistances for Nonflat and Polished Surfaces

To further evaluate the thermal resistance of TIM mating with a nonflat surface, effective thermal resistances of the metallized and polished TIM with finned zig zag micro-springs are compared with the thermal resistances of direct metal-to-metal contact interface for flat and nonflat surfaces, as shown in Figure 4.5 (b). The mating surfaces are same as the surface used for zig zag springs, which profile is shown in Figure 2.7 (a) and (b). Contact thermal resistances of direct metal-to-metal contact interface are 320 ± 10 and 1650 ± 40 $mm^2 \cdot K/W$, for flat and nonflat mating surface respectively. The thermal resistance increases by ~5 times due to the reduction of contact area. Effective thermal resistances of TIM are 280 ± 40 and 300 ± 40 $mm^2 \cdot K/W$, for flat and nonflat mating surface respectively. The thermal resistance change is lower than the uncertainty of measurement, which means the TIM performs similarly for different surface nonflatness as long as the compress pressure is large enough to deform it to conformally contact the surface. Note that the effective resistance of the TIM for flat surface is even lower than direct metal to metal contact resistance, which is caused by the little surface nonflatness of the nominally 'flat' surface.

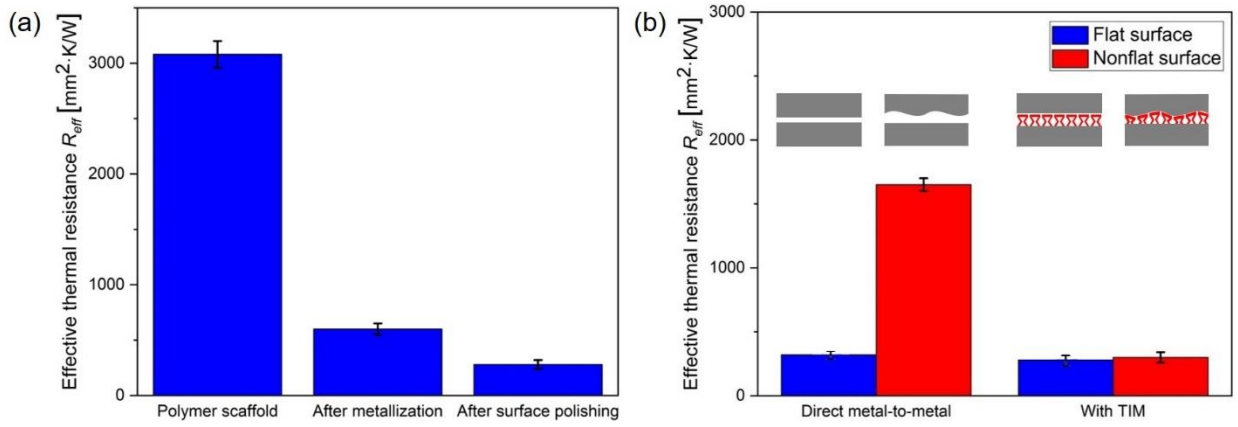

Figure 4.5 (a) Effective thermal resistances of the TIM for a flat and polished surface at three different fabrication stages: polymer scaffold, after metallization, and after surface polishing. (b) Comparison of the thermal resistances of a dry metal-to-metal interface, with and without the TIM inserted, for flat and nonflat polished mating surfaces. [49]

4.3.5 Effective Thermal Resistances of TIMs for a Flat and Rough Surface

To evaluate the influence of polymer coating for rough surface, a flat and rough surface made by standard machining is used as the mating surface, as shown in Figure 4.6 (a). There are ~100 scratches per millimeter on the surface, which generates a surface roughness of 0.52 μm characterized by an optical interferometer. The effective thermal resistances of metallized TIM with and without polymer coating are evaluated under a normal pressure of 20 kPa and compared to thermal resistances of direct metal-to-metal contact, as shown in Figure 4.6 (b). The direct metal-to-metal contact thermal resistance is 1280 ± 40 $mm^2 \cdot K/W$, while the effective thermal resistance of metallized TIM is 480 ± 50 $mm^2 \cdot K/W$. The metallized TIM still outperforms direct metal-to-metal contact for rough surface due to the soft polymer scaffold underneath but has ~70% higher thermal resistance than that for smooth surfaces which is 280 $mm^2 \cdot K/W$ shown in Figure 4.5 (a). After polymer coating, the effective thermal resistance is significantly reduced to 280 ± 35 $mm^2 \cdot K/W$, which is comparable to the resistance of TIM for flat and smooth surfaces.

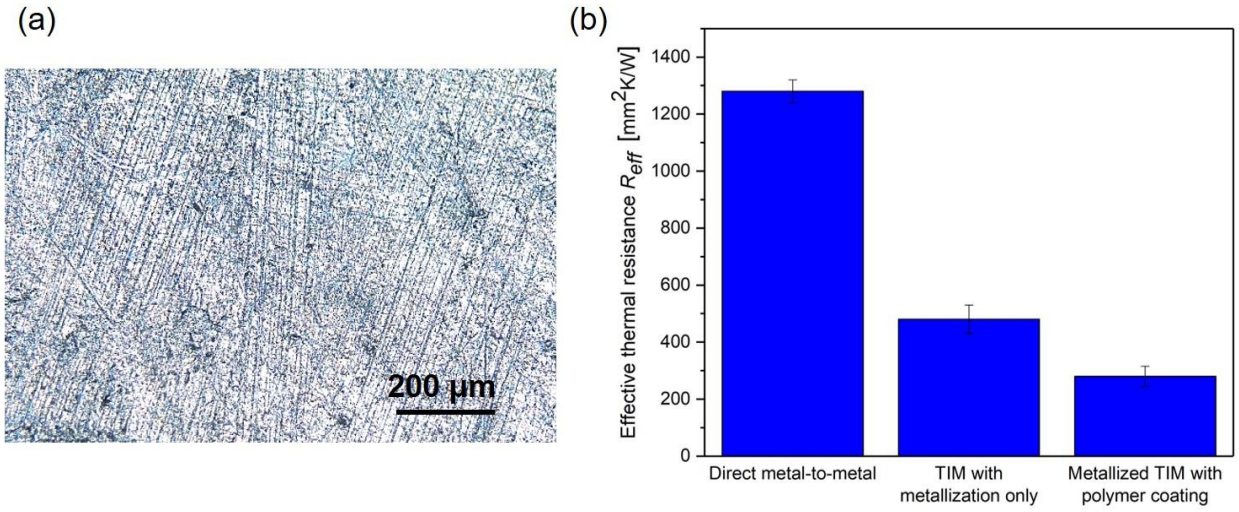

Figure 4.6 (a) Microscopic image of the flat and rough surface fabricated by standard machining. About 100 scratches per millimeter are exposed on the surface. (b) Comparison of thermal resistances of dry metal-to-metal contact without TIM, with metallized TIM inserted and with polymer-coated metallized TIM inserted. [49]

4.3.6 Effective Thermal Resistances Under Different Pressures

To evaluate the range of working pressures, effective thermal resistances of the metallized TIM for the flat and polished surface under different pressure (0~250 kPa), as shown in Figure 4.7. The metallized TIM has a large resistance of 1160 ± 100 $mm^2 \cdot K/W$ when unloaded which drops fast with the increasing pressures when the applied pressure is low. The resistance keeps almost consistent (differences within uncertainty) when the pressure is increasing to larger than 10 kPa. The metallized TIM can operate under a pressure up to 250 kPa, where the resistance is 250 ± 30 $mm^2 \cdot K/W$. Effective thermal resistances for nonflat and smooth surface are characterized under low pressures (0-20 kPa) range, as comparison to the flat surface. The metallized TIM have much higher thermal resistance (1680 ± 180 $mm^2 \cdot K/W$) for nonflat surface than flat surface at low pressure. The resistances for flat and nonflat surfaces converge at pressure of ~5 kPa when the TIM starts to conform to the nonflat surface.

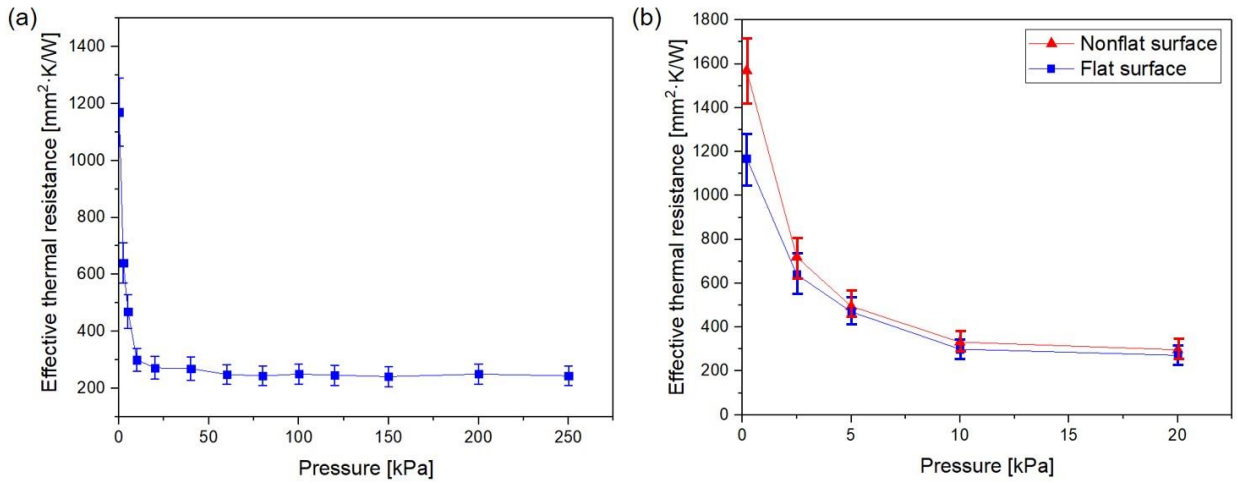

Figure 4.7 (a) Effective thermal resistances of the TIM with finned zig zag springs for a flat and smooth surface under different pressures (0-250 kPa). (b) Comparison of effective thermal resistances between a flat and a nonflat surface under different low pressures (0~20 kPa)

4.3.7 Reliability under Temperature Cycling

To evaluate early-stage reliability under repeated temperature change caused by switching on/off the device, a cycling test of the metallized TIM with finned zig zag micro-springs is

conducted by changing temperature between 20 – 90℃ for 15 times. The test is conducted for a flat and smooth mating surface under a compressive pressure of 20 kPa. The effective thermal resistance at each cycle is characterized as shown in Figure 4.8. The average effective thermal resistance is 280 ± 10 $mm^2 \cdot K/W$, and the effective thermal resistance changes in a small range of ± 5%, which confirms that there is no obvious performance degradation of the metallized TIM during temperature cycling.

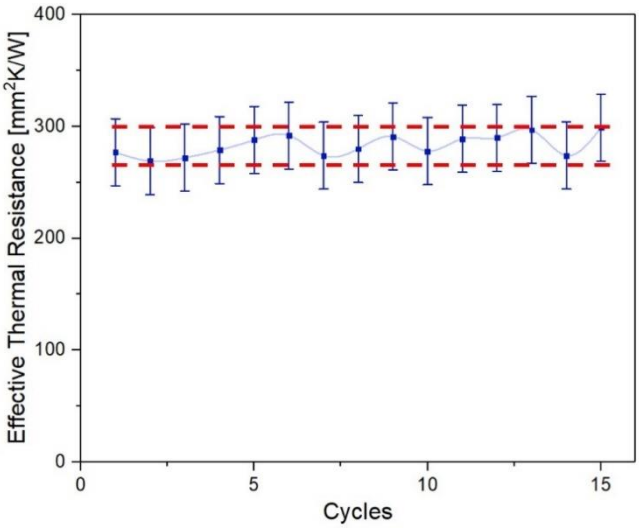

Figure 4.8 Effective thermal resistances of the metallized TIM with finned zig zag micro-springs at the end of each cycles when the TIM is heated and cooled for 15 times. The red dashed lines indicate the highest and lowest resistances during the cycling.

4.3.8 Mechanical Performance under Normal Compression

The mechanical performance of the metallized TIM with finned zig zag micro-springs under normal compression is characterized by using the experimental setup described in Section 2.2.4. The mechanical compliance of the TIM is evaluated by applying pressures up to 40 kPa. Figure 4.9 (a) shows the vertical displacements of the top surfaces of the micro-springs as a function of the applied pressures for two loading and unloading cycles. The metallized TIM can recover to its original height and has no hysteresis over this range of applied pressure in two cycles. The mechanical compliance is extracted from the data by using a linear fit, which is 2.35 μm/kPa. During the compression process, unlike the zig zag spring, the top surface of the finned zig zag

spring keeps consistent contact with the mating surface, due to the symmetric design as shown in the insets of Figure 4.9 (a).

4.3.9 Reliability under Normal Compression

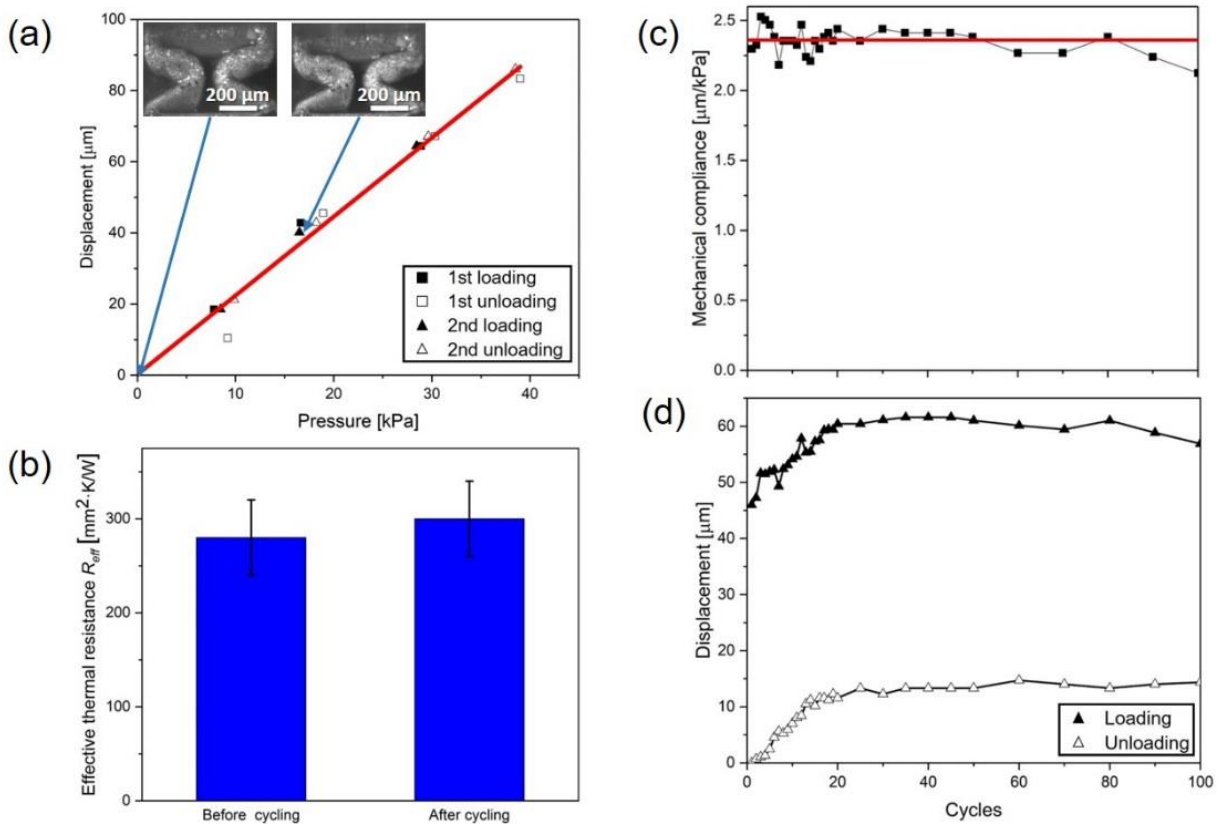

Figure 4.9 (a) Characterization of the vertical displacement as a function of the applied pressure of the metallized TIM with finned zig zag micro-springs: The solid line is the linear fit of the data. The slope of the solid line indicates mechanical compliance of the metallized TIM. The insets are microscopic images of a single metallized finned zig zag micro-spring under pressures of 0 kPa and ~20 kPa. (b) Mechanical compliance of the TIM during normal pressure cycling, the red line indicates the measured mechanical compliance (2.35 µm/kPa). (c) Effective thermal resistances of the TIM before and after cycling. (d) Vertical displacements when the metallized TIM is loaded and unloaded during cycling. The vertical displacement when unloaded indicates the plastic deformation of the TIM. [49]

To investigate the durability of the metallized TIM under normal pressures, a pressure of 20 kPa is applied and removed repeatedly to the metallized TIM with finned zig zag springs for 100 cycles. As shown in Figure 15b, the mechanical compliance keeps nearly constant during

pressure cycling. Figure 15c shows effective thermal resistances before and after cycling, which are almost same (the difference is within measurement uncertainty). There is no thermal performance degradation of the TIM after 100 pressure cycles. The vertical displacements of the TIM's top surface are recorded when the TIM is loaded (20 kPa) and unloaded (0 kPa), as shown in Figure 15d. The vertical displacement when unloaded indicates the plastic deformation of the TIM. In the first 20 cycles, the metallized TIM undergoes plastic deformation of 14 μm (3% of total height). After 20 cycles, the metallized TIM deforms elastically. These results confirm that the metallized TIM performs consistently in the early stage of usage under a pressure of 20 kPa.

4.3.10 Performance and Reliability under Sliding Contact

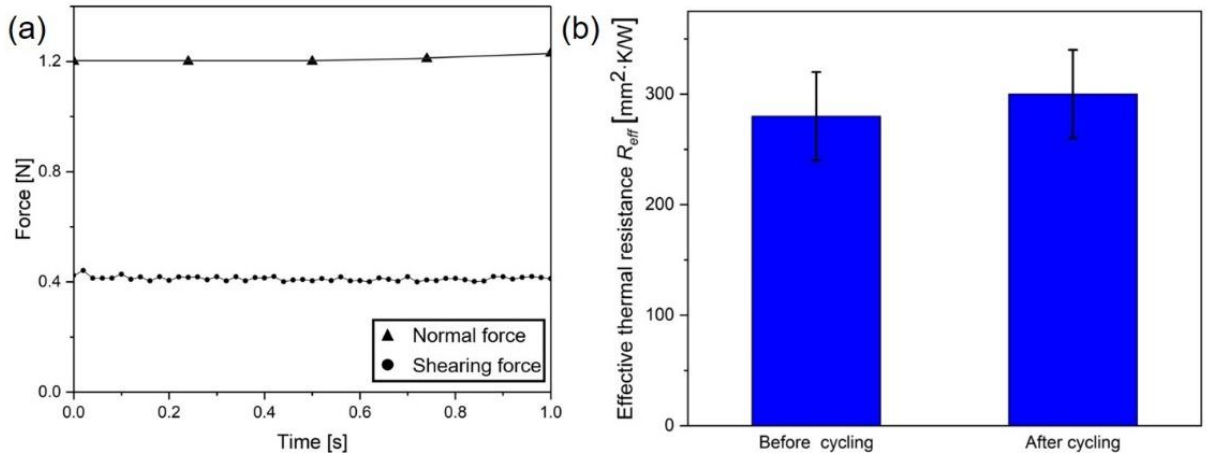

Figure 4.10 (a) The normal and shearing force applied on the metallized TIM during sliding with a glass slide. (b) Effective thermal resistances of the metallized TIM before and after 100 sliding contact cycles. [49]

The metallized TIM with finned zig zag micro-springs is moved against a glass slide, at a speed of 5 mm/s for a distance of 5 mm, to characterize it under the shearing force (circles) of sliding contact. The normal force (triangles) applied to the metallized TIM and the shear force during sliding contact are shown in Figure 4.10 (a). indicate the normal compression force. Both normal force and the shear force keep almost constant during sliding contact. The average normal force is 1.21 N, corresponding to a compressive pressure of 20 kPa. The average shear force is 0.41 N. The friction factor is ~0.3, which is higher than typical value of most interfaces.

To evaluate reliability of TIM under sliding contact, the metallized TIM is continuously moved back and force for 100 times, contacting with the glass slide under pressure of 20 kPa. The metallized TIM does not have obvious damage after cycling. As shown in Figure 4.10 (b), the effective thermal resistances of the metallized TIM before and after sliding is almost same (difference within measurement uncertainty). It confirms that, under a low pressure, the metallized TIM can survive repeated plugging without thermal performance degradation.

4.4 Thermal Demonstration on Pluggable Application

4.4.1 Integration of TIM on Pluggable Application

Direct fabrication of the micro-springs on the device surfaces (Figure 2.1 (b)) generates lowest thermal resistance which is almost same value of the effective thermal resistance. However, a base layer is required for the convenience of handling and transfer. High thermal resistances (R_b and $R_{c,bot}$) are introduced by the base layer, due to the low thermal conductivity of polymer and low contact thermal conductance between polymer base and metal device surface. Although the effective thermal resistance (R_{eff}) of the metallized TIM is low, the total insertion thermal resistance is still high, which disallows the metallized structure array to be directly applied between the surfaces as a TIM.

The resistances introduced by base layer (R_b and $R_{c,bot}$) are reduced to enhance the overall thermal conductance. As shown in Figure 4.11 (a), Through-holes (100 μm × 580 μm) near the feet of the micro-springs are created on the base layer of the polymer scaffold, which are coated with highly thermally conductive copper after metallization. The metal layer on the through-holes works as a conductive path for heat conduction to reduce R_b. A thin layer of epoxy (<10 μm) is applied and cured between the base layer and device surface to reduce $R_{c,bot}$.

To confirm the effect of these improved designs, total insertion thermal resistances of the TIM with finned zig zag micro-springs are measured with three different scenarios for a flat and polished surface: a solid polymer base with direct contact with the working surface, a solid polymer base with epoxy applied in between and the conductive base with through-holes and epoxy applied. As shown in Figure 4.11 (b), total insertion resistance of the metallized TIM with solid polymer base and direct contact with working surface is 1120 ± 30 $mm^2 \cdot K/W$. By applying a thin layer of epoxy, total resistance of metallized TIM is reduced to 560 ± 15 $mm^2 \cdot K/W$. The total resistance

of the TIM with conductive holes and epoxy applied is measured to be 350 ± 10 mm^2·K/W, which is comparable to thermal resistance of direct contact of polished and flat metal surfaces shown in Figure 4.7 (b). By applying epoxy and improved design of conductive holes, total resistance is reduced by 560 mm^2·K/W (Δ_1) and 210 mm^2·K/W (Δ_2), respectively.

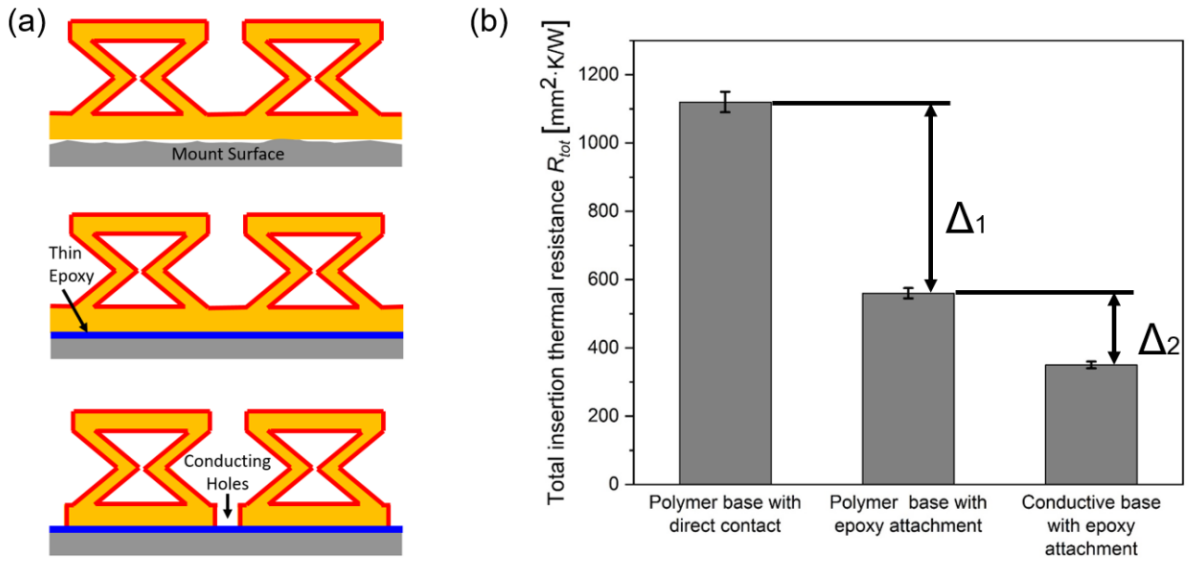

Figure 4.11 (a) Illustrations of the three tested scenarios for the TIM with finned zig zag micro-springs: a solid polymer base direct contacting the mount surface, a solid polymer base with epoxy applied in between and a base with conducting through-holes and epoxy applied. (b) Measured insertion thermal resistances (flat and polished surface, 20 kPa) for the three scenarios where Δ_1 indicates the resistance reduction by applying a thin layer of epoxy and Δ_2 indicates the resistance reduction by adding the thermally conducting through-holes. [49]

4.4.2 Thermal Demonstration on a Pluggable CFP4 Module

The performance of the TIM with finned zig zag micro-springs is thermally demonstrated on a CFP4 module. An experimental setup is established to thermally demonstrate the performance of the TIM by using the mating surface of CFP4 module, as shown in Figure 4.12 (a). A tightly arranged array of 2 × 9 fully-fabricated TIMs are boned upside down by thermal epoxy on the riding heatsink. The TIM-furnished heatsink is stacked on the mating surface of CFP4 module. The heat is generated by the heaters underneath the mating surface. A thermal insulation is used around the heater to minimize the heat loss. One thermocouple is set in a hole of the heat sink

which extracts the temperature of heat sink, and another thermocouple is set underneath the mating surface which represents the working temperature of CFP4 module.

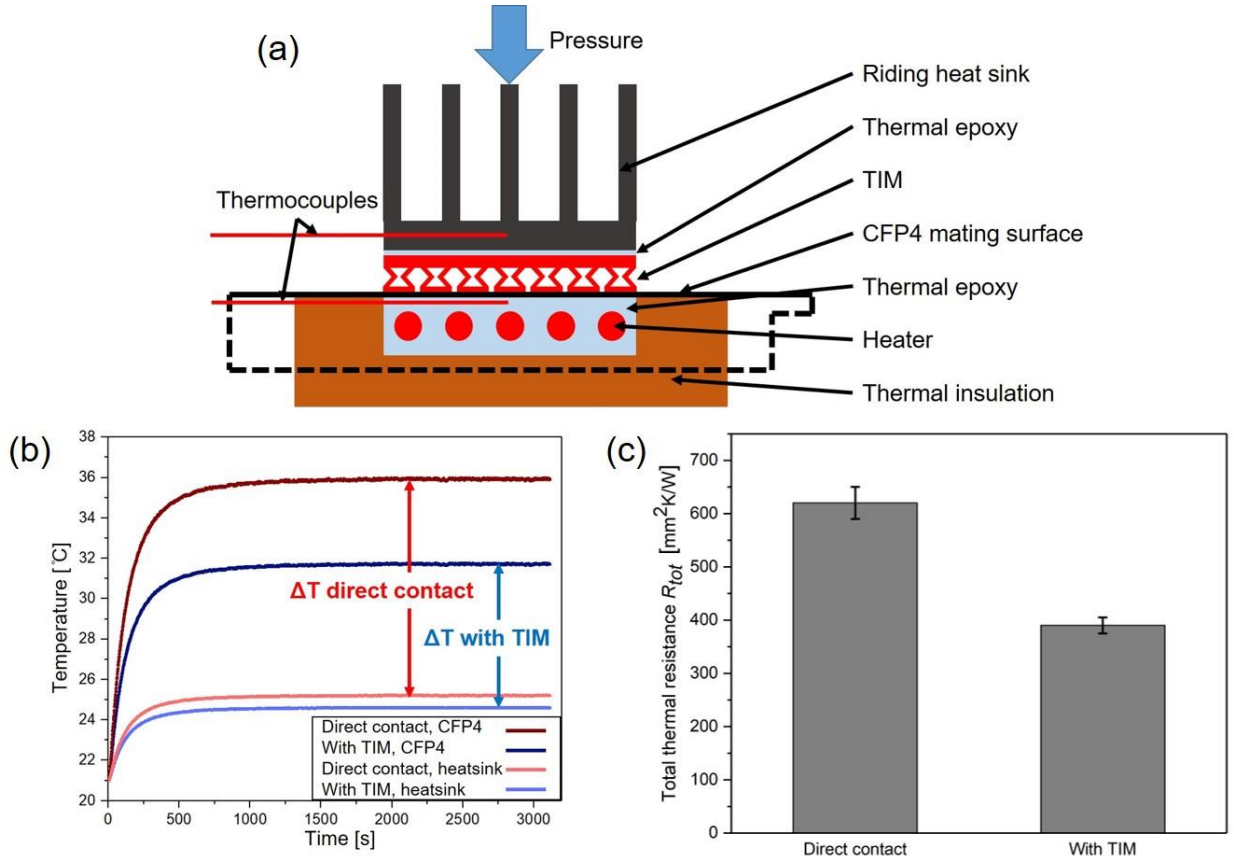

Figure 4.12 Schematic illustration of an experimental setup to demonstrate thermal performance of the TIM by using the mating surface of a CFP4 module. The dashed line indicates the outer shell of the CFP4 module mating with the riding heat sink. (a) Temperatures of CFP4 module and heat sink developing with time with and without the TIM inserted in the interface. (b) The total insertion thermal resistances with and without TIM inserted calculated from the temperature difference of CFP4 module and heat sink and the heating power.[50]

The thermal demonstration is conducted with heating power of ~5 W under a pressure of 20 kPa. The TIM is compared to the case where the mating surface directly contact the riding heat sink without any TIM inserted. The temperatures of the heatsink and CFP4 module are shown with timeline in Figure 4.12 (b). The steady temperatures of the heat sinks for both cases are almost same with the ambient temperature (~21˚C), while the temperature of the CFP4 module with TIM is lower than the module with direct contact. The total insertion thermal resistances of the TIM

and direct contact thermal resistance are calculated based on the temperature differences and the heating power, as shown in Figure 4.12 (b). The direct contact thermal resistance is 620 ± 30 $mm^2 \cdot K/W$, while the total insertion resistance of the TIM is 390 ± 15 $mm^2 \cdot K/W$, which is ~40% lower than the direct contact thermal resistance. The results confirm that the TIM enhances the contact thermal conductance and lower the working temperature of the CFP4 module. Note that the total insertion thermal resistance of the TIM here is higher than that for flat and smooth surface in Figure 4.11 (b) mainly because of exceptional materials (mating surface and a small portion of heat sink) and interfaces (epoxy-mating surface interface underneath) included in the total insertion resistances.

5. A NEAR ZERO STIFFNESS METAMATERIAL WITH PRE-STRESSED BEAMS

5.1 Introduction

In the previous chapters, a new type of micro-spring-based TIM has been demonstrated to work as TIMs for pluggable applications. There is always a tradeoff between thermal conductance and mechanical compliance for this spring-like structure. For example, thinner springs have better mechanical compliance, but lower thermal conductance; shorter springs have higher thermal conductance, but lower mechanical compliance. To decouple thermal conductance and mechanical compliance, a kind of structures and mechanisms with near zero stiffness so-called "zero stiffness materials" are investigated. Zero stiffness materials have been developed to solve the problem of undesirable mechanical vibrations [67-69], which can be used as vibration insulators for precision instruments in machinery, geodynamics and aerospace engineering [70-73]. In these structures, the zero stiffness is typically realized by using a combination of a positive stiffness component and a negative stiffness component.

Metamaterials with a negative stiffness have been widely studied and designed based on local resonance of microstructures, and variety of micro-structured materials have been designed and confirmed to have negative effective stiffness. Double negative (DNG) materials, with negative permittivity (ε) and negative permeability (μ), can lead to a negative refractive index of light, have drew intensive focus from the researchers due to the unique phenomena. The idea of DNG in an electromagnetic wave was proposed by Veselago [74] and the concept was demonstrated through the notion of metamaterial [75-77]. The electromagnetic (EM) metamaterials have been realized in practice which are composites with built-in resonance structures in some frequencies. In an acoustic wave, we can also engineer the dispersion relation of solids to achieve the same effect for phonons [78-80]. With this comparison, researchers are trying to find out whether we can have an analog of Veselago's medium in an acoustic wave whose effective mass and stiffness are "double negative". Since elastic waves and electromagnetic waves have much in common, the counterpart of optical DNG in elastic waves are widely studied, and bunch of micro-structured materials have been designed and confirmed to have negative effective mass and negative effective stiffness [81-83]. However, in these metamaterials, DNG are achieved

by utilizing the local resonance of microstructures, but the microstructures are built by normal materials which have intrinsic positive stiffness. These microstructures have positive stiffness under a quasi-static situation, which is not applicable in the case of thermal interface material.

Another type of negative stiffness component typically used in the near zero stiffness structures are bi-stable structures [84-90]. The negative stiffness is achieved during the transition between two stable states. Representative bi-stable components with negative stiffness are buckled [84-86] and curved beams [87, 88] exposed to transverse force. Compared to the buckled beam, the curved beam is more difficult to fabricate, but it does not require axial load, and have more design freedoms to control the state of negative stiffness.

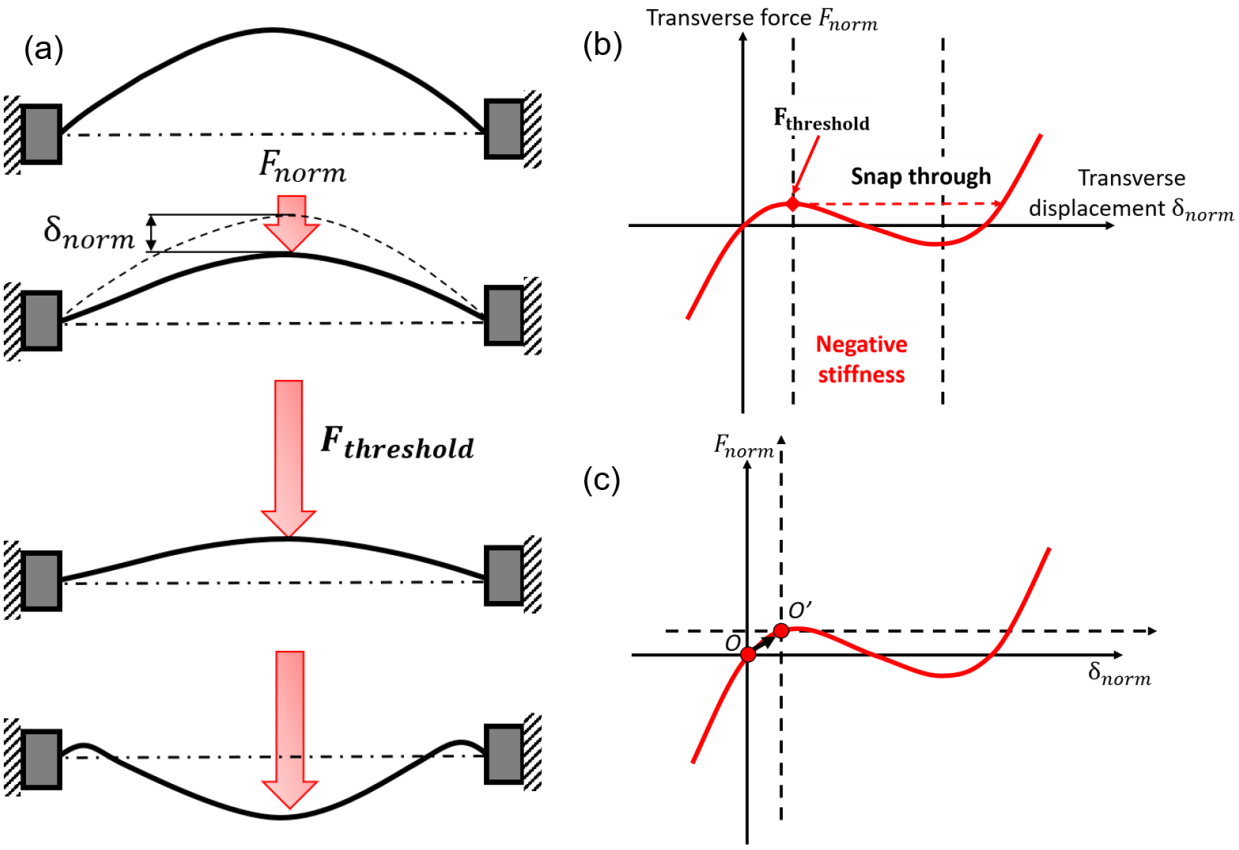

Figure 5.1. (a) The behavior of a curved beam when being compressed by a transverse force at its midpoint. (b) The relationship between transverse force and transverse displacement for a curved beam. (c) Illustration of the influence of residual stress initially built in the curved beam on the behavior of the curved beam under compression.

Consider a thin curved beam with two ends clamped. When an increasing transverse force F_{norm} is applied to the curved beam at its midpoint, the beam is slightly deflected at first; transverse displacement of the midpoint of the beam is δ_{norm}. When the transverse force reaches a certain value $F_{threshold}$, the beam suddenly changes its shape to a state when the midpoint of the beam moves to the other side of the centerline. The behavior of the curved beam under an increasing transverse force is shown in Figure 5.1 (a). Figure 5.1 (b) shows the transverse force applied on the curved beam to keep it stable at certain transverse displacement. The tangent slope of the curve reveals the stiffness of the curved beam. At first, the transverse force increases with the displacement, which shows a positive stiffness. After the transverse force reach its maxima, the force starts to decrease with the deflection, which shows a negative stiffness. By utilizing the curved beam, the negative stiffness can be achieved during compression. However, the curved beam does not initially have a negative stiffness where a dead load is required to compress the beam to the negative stiffness zone.

One way to build an elastic component with an initially negative stiffness is to apply residual stress to the curved beam during fabrication [86]. As shown in Figure 5.1 (c), the compression curve of a curved beam which is initially stress free is the red curve plotted in the solid coordinate of transverse force and transverse displacement. When an external compressive force is applied on the center of a curved beam, the state of compression moves along the compression curve from origin point *O* to point *O'*. Now consider a pre-stressed curved beam with the same internal residual stresses built in during fabrication, as the stress-free curved beam under compression. Since the pre-stressed beam have same compression state with the stress-free beam, the pre-stressed beam should experience the same compressive behavior as the stress-free beam after point *O'*. Therefore, the compression curve of the pre-stressed beam is the same red curve but plotted in a new coordinate (dashed) with origin at *O'*. In another word, by designing the residual stresses built in the curved beam, the compression curve can start at a certain point on the curve. This gives a possibility to build a curved beam with an initial negative stiffness by adding residual stresses to the structure. Under circumstance of force controlling, which is most cases in applications, the negative-stiffness element alone is not statically stable; the curved beam snaps through its centerline when the transverse force reaches a certain value ($F_{threshold}$). A component with a positive stiffness is required to hold the negative-stiffness element.

MEMS fabrication methods, such as deep-reactive ion etching (DRIE) [84] and single crystal reactive etching and metallization (SCREAM) [87], have been used to fabricate a near zero-stiffness structure. These fabrication techniques are good at building fine micro-structures in a few micrometers. However, these processes are complicated and time-consuming, where multiple steps of different operations are required. Besides, additive three-dimensional (3D) fabrication methods can build prototyped structures with complexed shapes. Selective laser sintering (SLS) has been used to fabricate near zero stiffness structures [85], but the size of the structure is 100 mm, which is not applicable for small instruments. On the other hands, in the previous work, the residual stresses are applied by hand or outer field, such as magnetic field, after the structure is fabricated, which is not convenient and not applicable for the cases where outer disturbance is undesirable.

In this report, an elastic metamaterial made of curved beams is designed and fabricated to have a near zero stiffness. Each unit of the metamaterial has a negative-stiffness curved beam and a positive-stiffness curved beam to stabilize it. A high-throughput and cost-effective micro-stereolithography (μSL) system and a procedure to build residual stress in the curved beam during fabrication is developed and applied to build the structure. Since the negative-stiffness beam cannot stand alone, stiffnesses of the combination of the two beams and the positive-stiffness beam alone are evaluated by measuring the displacements of the top of the beams under incrementally increasing compressive force to demonstrate the negative stiffness. Layered material built with different spatial arrangements of the beams are fabricated. Their behaviors under compression are characterized and demonstrate the variability and scalability of this kind of near zero stiffness metamaterial.

5.2 Methods

5.2.1 Design of the Near Zero Stiffness Micro-Structures

The near zero stiffness structure is designed to be a so-called ‘double curved beam’ as shown in Figure 5.2 (a). It consists of a positive stiffness top beam and a negative stiffness bottom beam. A stiff central bar connecting the top and bottom beams to convey compressive forces. Two side bars are designed to support the whole structure.

The plots of the relation between compression force and displacement of the top and bottom beams are shown in Figure 5.2 (b). Under compression, the top and bottom beams have same displacement due to the stiff central bar. We can add the curves of top and bottom beams to achieve the relation between compression force and displacement of the double curved beam. For the double curved beam, the compression force versus displacement curve first has a positive-stiffness step, which is caused by the stronger positive-stiffness top beam. During this step, both the positive-stiffness top beam and the negative-stiffness bottom beam are getting stronger, but the negative stiffness increases faster, so the curve is bending down. After reach a designed point when the positive and negative stiffnesses are equal, the curve enters a plateau of zero-stiffness where the compressive force increases little in a large range of displacement. Further increasing the compression force, the bottom beam becomes positive stiffness, and the curve goes up with a dramatically increasing slope. The double curved beam is expected to have a near zero stiffness under a certain amount of compression.

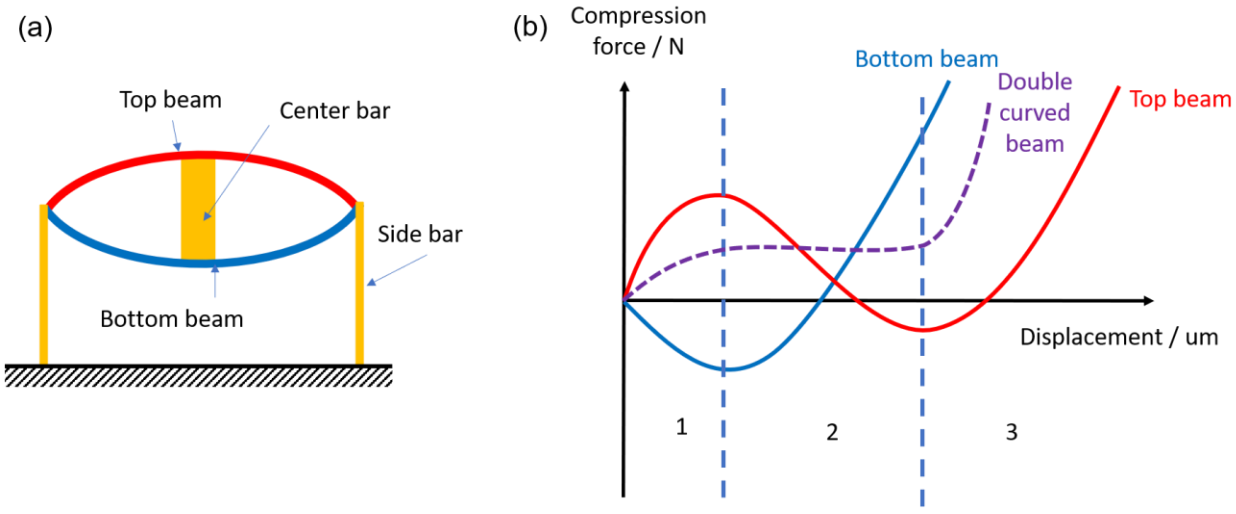

Figure 5.2. (a)Schematic illustration of designed near zero stiffness double curved beam. (b) Plot of the relation between compression force and displacement of the top (red) and bottom (blue) beams of the double curved beams, which contribute to that of double curved beam (dashed purple)

5.2.2 Fabrication of the Near Zero Stiffness Micro-Structures

The polymer scaffold of the TIM is built by using projection micro-stereolithography (μSL) technique as described in Section 2.2.2.

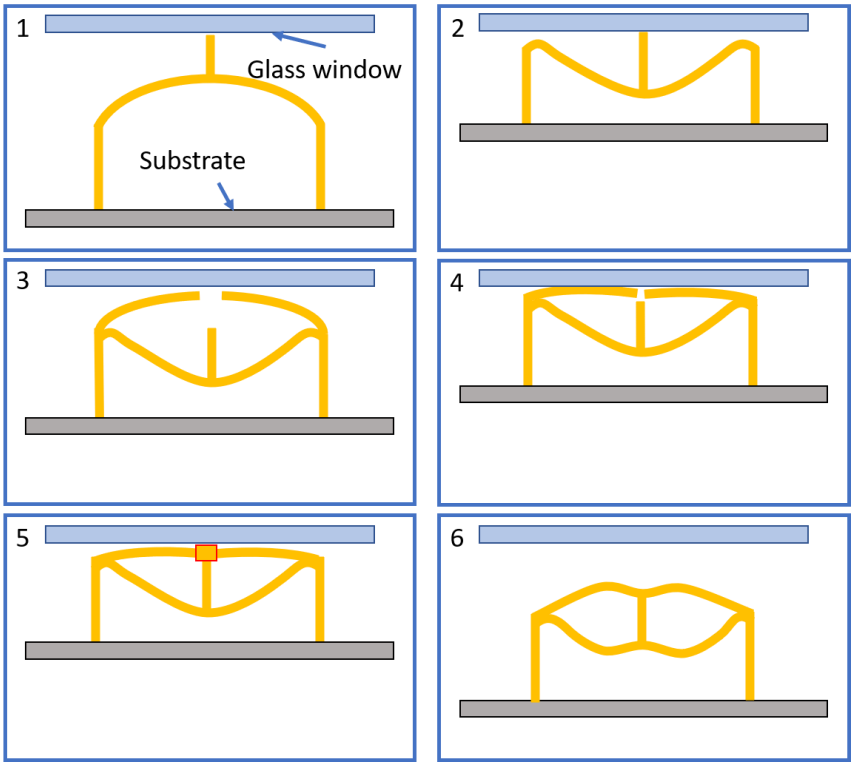

Figure 5.3. Illustration of the fabrication procedure to build the prestressed polymer double beam structure. The diagrams are the side view of the 3D double beam structure at each step during fabrication.

As mentioned in Section 5.1 and shown in Figure 5.1 (c), a negative stiffness curved beam is achievable by applying residual stress to the beam. In the setup shown in Figure 2.2 (a), it is possible to build residual stresses by compressing the beam with the cover glass. A fabrication procedure which includes compression is developed to build residual stresses in the structure, as shown in Figure 5.3. At first, the two supporting side bars, the bottom curved beam and central bar are first fabricated. The bottom beam initially bends up and the central bar is used to connecting the top and bottom beams. Then, the bottom beam is compressed to the bend-down stable state by the cover glass. After that, the top beam is fabricated without the top layers so that the two half-beams and the central bar are separated. The separated two top half-beams are compressed again

by the cover glass so that the ends of the two half-beams and the central bar come together. The top layers are fabricated under compression to merge the ends. After releasing the structure from compression, the top beam tends to go up to recover, but the bottom beam tends to maintain its stable state, which generates residual stresses in the beams. By designing the residual stress, the bottom beam can be moved into the negative stiffness zone, and the negative stiffness of the bottom beam is stable due to the constraint of the top beam. The residual stresses can be tuned by designing the distance of compression and the geometry of the beams. A near zero stiffness structure is achieved by engineering the positive and negative stiffness curved beams.

5.2.3 Experiment Measurement of Stiffness of Micro-Structures

To demonstrate the negative stiffness of the curved beam, the stiffnesses of the double curved beam structure is characterized by an experimental setup shown in Figure 2.3. The test procedure is described in Section 2.2.4.

5.3 Results

5.3.1 Demonstration of Near Zero Stiffness of the Designed Micro-Structures

The side view photo of one double curved beam is shown in Figure 5.4 (a). The curved beam has an overall span of 1 mm, height of 400 μm and thickness of 40 μm. The middle regions of the top and bottom beams are bent downwards due to the intentional residual stresses. To build a metamaterial, the double curved beams are arranged in a 6 × 3 array with the side supporting bars connected to its neighbors, as shown in Figure 5.4 (b).

The array of double curved beams is compressed in the setup shown in Figure 2.3. Plots of the compression force versus displacement are shown in Figure 5.4 (c). No snap-through happened during the compression of the double curved beams, and the double curved beams can recover to their original state without hysteresis. The slope of the curves in the plot indicates the stiffness of the beams. Without any compression, the double curved beams have positive stiffness. With the compressive force increasing, the stiffness decreases. The stiffness decreases to near zero until the compressive force increases to 0.43 N. After that, the compressive force increases only 0.6 N, while the displacement increases ~350 μm, which indicates a near zero stiffness. The stiffness

increases dramatically after the compressive force reaches 0.49 N. The behavior of the double curved beam indicates that this structure has a near zero stiffness zone under a certain amount of compression

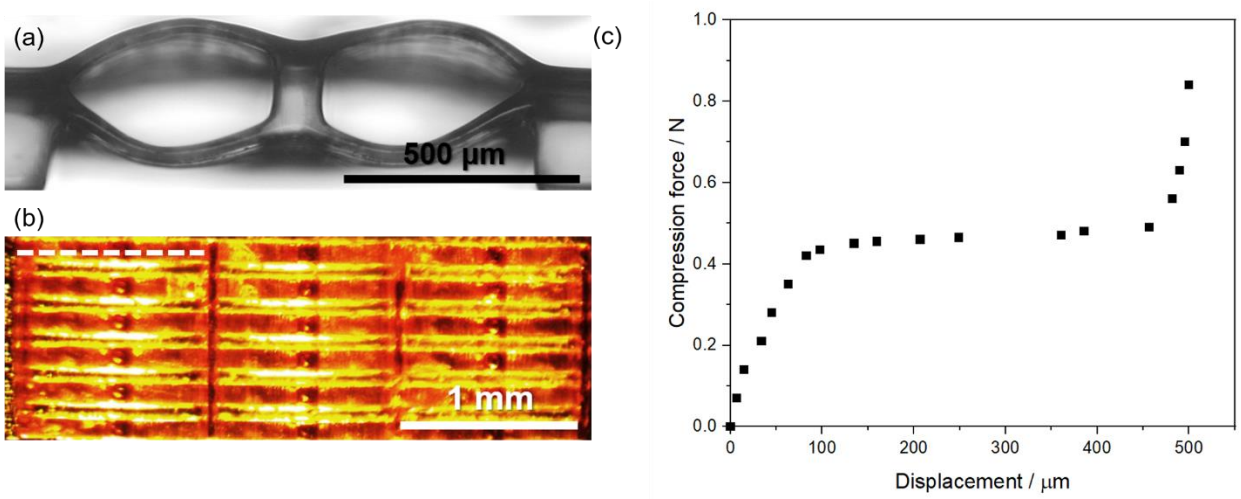

Figure 5.4. (a) Side view microscope images of a one double curved beam micro-structure. (b) Top view microscope images of the array of the double curved beam micro-structure. The dashed line indicates one single micro-structure in the array. (c) Plot of the compression force versus displacement of arrays of double curved beams and single curved beams. The single curved beams, which are same as the top positive-stiffness beams in the double curved beams, have larger stiffness than the double curved beam. The results indicate a negative stiffness of the bottom beams in the double curved beams.

5.3.2 Layered Zero-Stiffness Material

To build a layered zero-stiffness material, the zero-stiffness double curved beams are arranged in two ways as shown in in Figure 5.5 (a) and (b). As shown in Figure 5.5 (a), three double curved beam structures form a triangle shape in one layer with their sides connected. One layer of such structures lies on another layer with the side bars of the top layer sitting on the central bars of the bottom layer. In this structure, each layer shifts a distance of half of the beams from its bottom layer. 1/3 of the beam structures (red) in the bottom layer is in the direction of shifting, which are connected with the top layer by the side bars, while in the other directions, the structures (blue) in the bottom layer are not connected with the top layer. The other arrangement is shown in in Figure 5.5 (b). Six half-beams of the double curved beam structures are arranged in a hexagon

structure in each layer with their side bars and central bars connected. One layer of such structures lies on another layer with the side bars of the top layer sitting on the central bars of the bottom layer. In this arrangement, all the beam structures in the bottom layer are connected with the top layer.

The two kinds of zero-stiffness material with arrangement a and b with 1 and 2 layers are compressed and the compression curves are shown in in Figure 5.5 (c). The colors of dots represent the arrangements, with red for arrangement (a), blue for (b). The shapes of the dots represent how many layers in the materials, with circle for single layer material, triangle for double. Both of the single-layer structures with arrangement (a) and (b) behave similarly. Only the forces to enter the zero-stiffness plateau are different due to the filling ratio of the beam structures. For double-layer structure with arrangement (a), as mentioned before, only the structures on the bottom layer in the direction of shifting, which is about 1/3 of the total, are connected to the structures on the top. When the double-layer structure with arrangement (a) is under compression, the structures in the top layer are all under compressions, while only 1/3 of the structures in the bottom are under compression. With the increasing of compressive force, the structures in the bottom layer are first compressed to the zero-stiffness plateau with about 1/3 of the compressive force to enter the zero-stiffness plateau of single-layer structures. Since structures are all arranged in the same way, the distances of the zero-stiffness plateaus of the single-layer structure with arrangement (a), the first and second plateaus of the double -layer structure with arrangement (a) have same length. For double-layer structure with arrangement (b), the behavior under compression is similar with its single-layer version. The plateau of double-layer structure with arrangement b is about twice as long as the single-layer one, which show the zero-stiffness plateau is scalable by changing the number of layers. For double-layer structure (a), the curve shows two zero-stiffness plateaus.

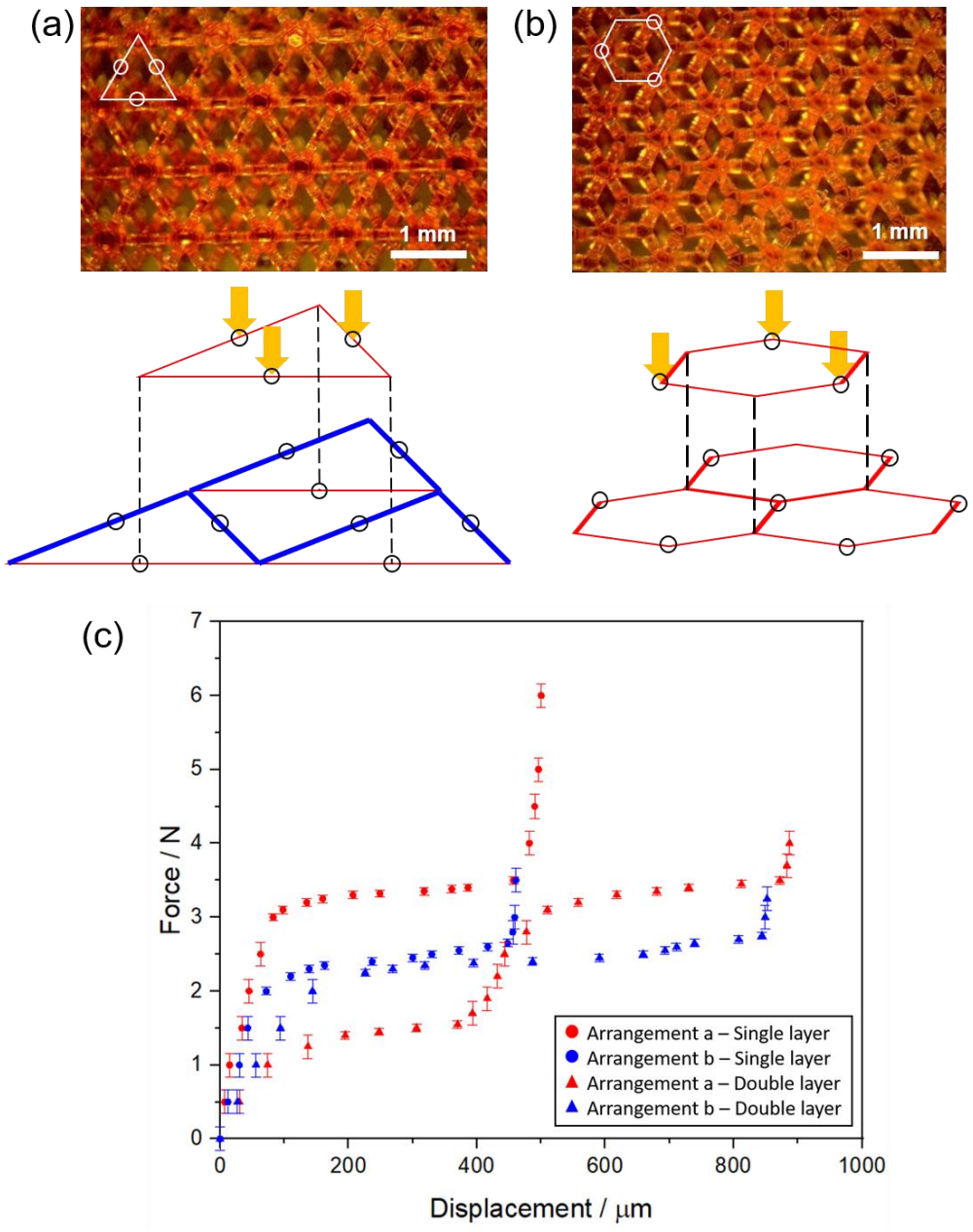

Figure 5.5. (a, b) Top view microscope images of the layered zero-stiffness materials with two kinds of arrangement and schematic illustration of the vertical arrangement of the layered materials. In the schematic illustration, the circles are the positions of the central bars in the double curved beam structures; the dashed lines are the side bars connecting the two layers; the red lines are the double curved beam structures under compression, while the blue lines are the beam structures which are not compressed. (c) The compression force versus displacement curve of zero-stiffness materials. The colors of dots represent the arrangements, with red for arrangement a, blue for b. The shapes of the dots represent how many layers in the materials, with circle for single layer material and triangle for double.

6. CONCLUSIONS

In this dissertation, compliant microstructure arrays are demonstrated as a thermal interface material (TIM) to enhance dry contact thermal conductance across nonflat interfaces under low pressures of a few to a few hundreds of kPa. A soft zig zag micro-spring array is originally designed to solve the problem. Projection micro-stereolithography is used to fabricate the microscale polymer spring structures designed for high compliance; this polymer scaffold is metallized to enhance the thermal conductance of the structures. This TIM is demonstrated to exhibit high mechanical compliance. Furthermore, thermal resistance tests using flat and nonflat surfaces demonstrate that the effective resistance of this dry TIM is nearly unaffected by the surface nonflatness; this is in stark contrast with direct metal-to-metal interfaces that have a thermal resistance value strongly coupled with the nonflatness. This work demonstrated the possibility for designing and creating large-scale microstructured TIMs for dry contact interfaces under low pressures.

To enhance the thermomechanical performances of the micro-structured TIM, a centrosymmetric hexagon spring is designed as TIM for pluggable applications. Compared to originally designed zig zag springs, the centrosymmetric hexagon spring does not have the undesired tip rotation under compressive pressures and therefore remains in contact with the mating surface during compression, which is confirmed by simulations and experimental observations. Experimental measurements of the mechanical compliance of polymer hexagon springs show reasonable agreements with simulation-based predictions of the compliance, which demonstrated the capability to fabricate the hexagon spring to a design-targeted compliance. Thermal resistance measurements for flat and nonflat mating surfaces show that the effective thermal resistance of the copper-coated hexagon spring array is unaffected by the surface nonflatness, unlike the direct metal-to-metal contact which has extreme sensitivity to the nonflatness of the opposing surface. This work shows the possibility to design and create a metallized microstructure as a TIM for dry contact under low pressures.

To further enhance the thermal conductance, a symmetric finned zig zag micro-spring geometry is designed. Projection micro-stereolithography (μSL) is used to create the compliant polymer scaffold. An electroless metal plating method, with etching-free activation, is used to coat

the polymer scaffold with metal to improve the thermal conductance of the micro-spring array. The effective resistance of this metallized TIM is measured to be 280 ± 40 $mm^2 \cdot K/W$. Thermal resistances tests conducted for both flat and nonflat mating surfaces confirm the effective thermal resistance of the TIM is nearly unaffected by surface nonflatness and significantly outperforms direct metal-to-metal contact between nonflat surfaces. Mechanical cycling tests under normal pressure and sliding contact confirm the early-stage durability of the metallized TIM. In addition to fabricating directly it onto a working surface, an insertion approach is demonstrated for which the metallized TIM can be fabricated with a conductive base layer and used as an attachable TIM that is affixed to the surface. To accommodate microscale surface roughness, we coat a thin layer of soft polymer on the metallized TIM. Thermal resistance characterization using rough mating surfaces (~0.5 μm) confirms that this polymer coating conforms to surface roughness and reduces the thermal resistance under a compressive pressure of 20 kPa. The polymer-coated metallized TIM is then demonstrated to enhance the contact thermal conductance between a CFP4 module mating surface and its riding heat sink. The thermal and mechanical reliability of the TIM is evaluated by sliding the TIM against a CFP4 module surface for 100 cycles at the compressive pressure required of pluggable applications.

To decouple mechanical compliance and thermal conductance, a new type of zero stiffness structure of stable double curved beams composed of negative and positive stiffness elastic elements is designed and fabricated by introducing residual stresses. The compressive forces applied on the structures and the displacements are characterized which show that the positive-stiffness single curved beam, which is same as the top beam in the double curved beam, is stiffer than the double curved beam. This confirms the negative stiffness of the bottom beam in the double curved beam. Layered near zero-stiffness structures are designed and built to demonstrate the scalability of these double curved beam structures. More than one zero-stiffness zone at different compressive forces can be achieved by the double-layer structure with a triangle arrangement. The behavior of the double-layer structure with a hexagonal arrangement demonstrates that the length of the zero stiffness zone can be tuned by changing the number of layers

REFERENCES

1. Marotta, E., & Fletcher, L. S. (1996). Thermal contact conductance of selected polymeric materials. *Journal of Thermophysics and Heat Transfer*, 10(2), 334–342.
2. Mahajan, R. V., Patel, P. R., Mallik, D., Tang, J., Wakharkar, V. S., Chrysler, G. M., … Viswanath, R. S. (2003). Critical Aspects of High-Performance Microprocessor Packaging. *MRS Bulletin*, 28(1), 21–34.
3. Garimella, S. V., Fleischer, A. S., Murthy, J. Y., Keshavarzi, A., Prasher, R., Patel, C., … Raad, P. E. (2008). Thermal Challenges in Next-Generation Electronic Systems. *IEEE Transactions on Components and Packaging Technologies*, 31(4), 801–815.
4. Cooper, M. G., Mikic, B. B., & Yovanovich, M. M. (1969). Thermal contact conductance. *International Journal of Heat and Mass Transfer*, 12(3), 279–300.
5. Madhusudana, C.V. and Ling, F.F. (1996). *Thermal Contact Conductance* (pp. 1-43), New York: Springer-Verlag.
6. Yeh, L.T. and Chu, R.C. (2002). *Thermal Management of Microelectronic Equipment*, New York: ASME.
7. Fletcher, L. S. (1990). A review of thermal enhancement techniques for electronic systems. *InterSociety Conference on Thermal Phenomena in Electronic Systems* (pp. 136–148).
8. Prasher, R. (2006). Thermal Interface Materials: Historical Perspective, Status, and Future Directions. *Proceedings of the IEEE*, 94(8), 1571–1586.
9. Hansson, J., Nilsson, T. M. J., Ye, L., & Liu, J. (2018). Novel nanostructured thermal interface materials: a review. *International Materials Reviews*, 63(1), 22–45.
10. Antonetti, V. W., & Yovanovich, M. M. (1985). Enhancement of Thermal Contact Conductance by Metallic Coatings: Theory and Experiment. Journal of Heat Transfer, 107(3), 513–519.
11. LAMBERT, M. A., & FLETCHER, L. S. (1993). Review of the thermal contact conductance of junctions with metalliccoatings and films. *Journal of Thermophysics and Heat Transfer*, 7(4), 547–554.
12. Merrill, C. T., & Garimella, S. V. (2011). Measurement and Prediction of Thermal Contact Resistance Across Coated Joints. *Experimental Heat Transfer*, 24(2), 179–200.
13. Prasher, R. S. (2001). Surface Chemistry and Characteristics Based Model for the Thermal Contact Resistance of Fluidic Interstitial Thermal Interface Materials. *Journal of Heat Transfer*, 123(5), 969–975.
14. Narumanchi, S., Mihalic, M., Kelly, K., & Eesley, G. (2008). Thermal interface materials for power electronics applications. *2008 11th Intersociety Conference on Thermal and Thermomechanical Phenomena in Electronic Systems* (pp. 395–404).
15. Viswanath, R., Wakharkar, V., Watwe, A., Lebonheur, V., Group, M., & Corp, I. (2000). Thermal Performance Challenges from Silicon to Systems. *Intel Technol J. Q3*, 1–16
16. Bar-Cohen, A., Matin, K. and Narumanchi, S. (2015). Nanothermal interface materials: technology review and recent results. *Journal of Electronic Packaging*, 137(4), p.040803.

17. McNamara, A.J., Joshi, Y. and Zhang, Z.M. (2012). Characterization of nanostructured thermal interface materials–a review. *International Journal of Thermal Sciences*, 62, pp.2-11.
18. Ishida, H. and Rimdusit, S. (1998). Very High Thermal Conductivity Obtained by Boron Nitride-Filled Polybenzoxazine. *Thermochimica Acta*, 320, no. 1: 177–86.
19. Yu, H., Li, L., Kido, T., Xi, G., Xu, G., & Guo, F. (2012). Thermal and insulating properties of epoxy/aluminum nitride composites used for thermal interface material. *Journal of Applied Polymer Science*, 124(1), 669–677.
20. Xu, J., Munari, A., Dalton, E., Mathewson, A., & Razeeb, K. M. (2009). Silver nanowire array-polymer composite as thermal interface material. *Journal of Applied Physics*, 106(12), 124310.
21. Wang, S., Cheng, Y., Wang, R., Sun, J., & Gao, L. (2014). Highly Thermal Conductive Copper Nanowire Composites with Ultralow Loading: Toward Applications as Thermal Interface Materials. *ACS Applied Materials & Interfaces*, 6(9), 6481–6486.
22. Hong, W.-T., & Tai, N.-H. (2008). Investigations on the thermal conductivity of composites reinforced with carbon nanotubes. *Diamond and Related Materials*, 17(7), 1577–1581.
23. Tang, B., Hu, G., Gao, H., & Hai, L. (2015). Application of graphene as filler to improve thermal transport property of epoxy resin for thermal interface materials. *International Journal of Heat and Mass Transfer*, 85, 420–429.
24. Choi, E. S., Brooks, J. S., Eaton, D. L., Al-Haik, M. S., Hussaini, M. Y., Garmestani, H., Li, D., & Dahmen, K. (2003). Enhancement of thermal and electrical properties of carbon nanotube polymer composites by magnetic field processing. *Journal of Applied Physics*, 94(9), 6034–6039.
25. Marconnet, A. M., Yamamoto, N., Panzer, M. A., Wardle, B. L., & Goodson, K. E. (2011). Thermal Conduction in Aligned Carbon Nanotube–Polymer Nanocomposites with High Packing Density. *ACS Nano*, 5(6), 4818–4825.
26. Iijima, S. (1991). Helical microtubules of graphitic carbon. *Nature*, 354, pp.56-58.
27. Marconnet, A.M., Panzer, M.A., & Goodson, K.E. (2013). Thermal conduction phenomena in carbon nanotubes and related nanostructured materials. *Reviews of Modern Physics*, 85(3), p.1295.
28. Wasniewski, J.R., Altman, D.H., Hodson, S.L., Fisher, T.S., Bulusu, A., Graham, S., & Cola, B.A. (2012). Characterization of metallically bonded carbon nanotube-based thermal interface materials using a high accuracy 1D steady-state technique. *Journal of Electronic Packaging*, 134(2), p.020901.
29. Lin, W., Zhang, R., Moon, K.S., & Wong, C.P. (2010). Synthesis of high-quality vertically aligned carbon nanotubes on bulk copper substrate for thermal management. *IEEE Transactions on Advanced Packaging*, 33(2), pp.370-376.
30. Shaddock, D., Weaver, S., Chasiotis, I., Shah, B., & Zhong, D. (2011). Development of a compliant nanothermal interface material. *ASME InterPack*, IPACK2011-52015.
31. Kempers, R., Lyons, A.M., & Robinson, A.J. (2014). Modeling and experimental characterization of metal microtextured thermal interface materials. *Journal of Heat Transfer*, 136(1), p.011301.

32. Feng, B., Faruque, F., Bao, P., Chien, A., Kumar, S., & Peterson, G. P. (2013) Double-Sided Tin Nanowire Arrays for Advanced Thermal Interface Materials. *Applied Physics Letters*, 102, no. 9: 093105.
33. Barako, M.T., Roy-Panzer, S., English, T.S., Kodama, T., Asheghi, M., Kenny, T.W., & Goodson, K.E. (2015). Thermal Conduction in Vertically Aligned Copper Nanowire Arrays and Composites. *ACS Applied Materials & Interfaces*, 7, no. 34: 19251–59.
34. OIF-Thermal-01.0, (2015). Implementation Agreement for Thermal Interface Specification for Pluggable Optics Modules. *Optical Internetworking Forum*.
35. CFP MSA, (2014). CFP4 Hardware Specification.
36. Raza, M. A., Westwood, A. V. K., Stirling, C., & Ahmad, R. (2015). Effect of boron nitride addition on properties of vapour grown carbon nanofiber/rubbery epoxy composites for thermal interface applications. *Composites Science and Technology*, *120*, 9-16.
37. Raza, M. A., Westwood, A. V. K., Brown, A. P., & Stirling, C. (2012). Performance of graphite nanoplatelet/silicone composites as thermal interface adhesives. *Journal of Materials Science: Materials in Electronics*, *23*(10), 1855-1863.
38. Xu, J., Munari, A., Dalton, E., Mathewson, A., & Razeeb, K. M. (2009). Silver nanowire array-polymer composite as thermal interface material. *Journal of Applied Physics*, *106*(12), 124310.
39. Yu, H., Li, L., & Zhang, Y. (2012). Silver nanoparticle-based thermal interface materials with ultra-low thermal resistance for power electronics applications. *Scripta Materialia*, *66*(11), 931-934.
40. Roy, C. K., Bhavnani, S., Hamilton, M. C., Johnson, R. W., Nguyen, J. L., Knight, R. W., & Harris, D. K. (2015). Investigation into the application of low melting temperature alloys as wet thermal interface materials. *International Journal of Heat and Mass Transfer*, *85*, 996-1002.
41. Cola, B. A., Xu, J., Cheng, C., Xu, X., Fisher, T. S., & Hu, H. (2007). Photoacoustic characterization of carbon nanotube array thermal interfaces. *Journal of applied physics*, *101*(5), 054313.
42. Hodson, S. L., Bhuvana, T., Cola, B. A., Xu, X., Kulkarni, G. U., & Fisher, T. S. (2011). Palladium thiolate bonding of carbon nanotube thermal interfaces. *Journal of electronic packaging*, *133*(2).
43. Kempers, R., Lyons, A. M., & Robinson, A. J. (2014). Modeling and experimental characterization of metal microtextured thermal interface materials. *Journal of heat transfer*, *136*(1).
44. Feng, B., Faruque, F., Bao, P., Chien, A. T., Kumar, S., & Peterson, G. P. (2013). Double-sided tin nanowire arrays for advanced thermal interface materials. *Applied Physics Letters*, *102*(9), 093105.
45. Wasniewski, J. R., Altman, D. H., Hodson, S. L., Fisher, T. S., Bulusu, A., Graham, S., & Cola, B. A. (2012). Characterization of metallically bonded carbon nanotube-based thermal interface materials using a high accuracy 1D steady-state technique. *Journal of Electronic Packaging*, *134*(2).
46. https://www.laird.com/thermal-interface-materials/thermal-gap-fillers/tflex-300
47. Cui, J., Wang, J., Zhong, Y., Pan, L., & Weibel, J. A. (2018). Metallized compliant 3D microstructures for dry contact thermal conductance enhancement. *Journal of Micromechanics and Microengineering*, 28(5), 055005.

48. Cui, J., Weibel, J. A., & Pan, L. (2018). Metallized Three-Dimensional Centrosymmetric Microstructures to Enhance Dry Contact Thermal Conductance across Nonflat Interfaces. *The 16th International Heat Transfer Conference (IHTC)*, IHTC16-23666.
49. Cui, J., Wang, J., Weibel, J. A., & Pan, L. (2019). A compliant microstructured thermal interface material for dry and pluggable interfaces. *International Journal of Heat and Mass Transfer*, 131, 1075–1082.
50. Cui, J., Pan, L., & Weibel, J. A. (2020). Demonstration of a Compliant Microspring Array as a Thermal Interface Material for Pluggable Optoelectronic Transceiver Modules. *Journal of Electronic Packaging*, *142*(3).
51. Sugioka, K., & Cheng, Y. (2014). Femtosecond laser three-dimensional micro-and nanofabrication. *Applied physics reviews*, *1*(4), 041303.
52. Kawata, S., Sun, H. B., Tanaka, T., & Takada, K. (2001). Finer features for functional microdevices. *Nature*, *412*(6848), 697-698.
53. Zhang, X., Jiang, X. N., & Sun, C. (1999). Micro-stereolithography of polymeric and ceramic microstructures. *Sensors and Actuators A: Physical*, *77*(2), 149-156.
54. Fischer, J., & Wegener, M. (2011). Three-dimensional direct laser writing inspired by stimulated-emission-depletion microscopy. *Optical Materials Express*, *1*(4), 614-624.
55. Farsari, M., & Chichkov, B. N. (2009). Two-photon fabrication. *Nature photonics*, *3*(8), 450-452.
56. Choi, J. W., Wicker, R., Lee, S. H., Choi, K. H., Ha, C. S., & Chung, I. (2009). Fabrication of 3d biocompatible/biodegradable micro-scaffolds using dynamic mask projection microstereolithography. *Journal of Materials Processing Technology*, 209(15–16), 5494-5503.
57. Zheng, X., Deotte, J., Alonso, M.P., Farquar, G.R., Weisgraber, T.H., Gemberling, S., Lee, H., Fang, N., & Spadaccini, C.M. (2012). Design and optimization of a light-emitting diode projection micro-stereolithography three-dimensional manufacturing system. Review of Scientific Instruments, 83(12), p.125001.
58. Bao, Y., He, C., Zhou, F., Stuart, C., & Sun, C. (2012). A realistic design of three-dimensional full cloak at terahertz frequencies. *Applied Physics Letters*, 101(3), p.031910.
59. Lin, D., Nian, Q., Deng, B., Jin, S., Hu, Y., Wang, W., & Cheng, G.J. (2014). Three-dimensional printing of complex structures: man made or toward nature? *ACS Nano*, 8(10), pp.9710-9715.
60. Chen, Q., Xu, R., He, Z., Zhao, K., & Pan, L. (2017). Printing 3d gel polymer electrolyte in lithium-ion microbattery using stereolithography. *Journal of the Electrochemical Society*, 164(9), A1852-A1857.
61. Ha, Y. M., Choi, J. W., & Lee, S. H. (2008). Mass production of 3-d microstructures using projection microstereolithography. *Journal of Mechanical Science & Technology*, 22(3), 514.
62. Sun, C., Fang, N., Wu, D.M., & Zhang, X. (2005). Projection micro-stereolithography using digital micro-mirror dynamic mask. *Sensors and Actuators A: Physical*, 121(1), pp.113-120.
63. Meza, L.R., Das, S., & Greer, J.R. (2014). Strong, lightweight, and recoverable three-dimensional ceramic nanolattices. *Science*, 345(6202), pp.1322-1326.

64. Soukoulis, C.M., & Wegener, M. (2011). Past achievements and future challenges in the development of three-dimensional photonic metamaterials. *Nature Photonics*, 5(9), pp.523-530.
65. Mallory, G.O., & Hajdu, J.B. (1990). *Electroless plating: fundamentals and applications*, William Andrew.
66. Lim, V. W. L., Kang, E. T., & Neoh., K. G. (2001). Electroless Plating of Palladium and Copper on Polypyrrole Films. *Synthetic Metals*, 123, no. 1: 107–15.
67. Carrella, A., Brennan, M. J., & Waters, T. P. (2007). Static analysis of a passive vibration isolator with quasi-zero-stiffness characteristic. *Journal of sound and vibration*, *301*(3-5), 678-689.
68. Kovacic, I., Brennan, M. J., & Waters, T. P. (2008). A study of a nonlinear vibration isolator with a quasi-zero stiffness characteristic. *Journal of sound and vibration*, *315*(3), 700-711.
69. Liu, X., Huang, X., & Hua, H. (2013). On the characteristics of a quasi-zero stiffness isolator using Euler buckled beam as negative stiffness corrector. *Journal of Sound and Vibration*, *332*(14), 3359-3376.
70. Denoyer, K. K., & Johnson, C. D. (2001). Recent achievements in vibration isolation systems for space launch and on-orbit applications. In *IAF, International Astronautical Congress, 52 nd, Toulouse, France*.
71. DANKOWSKI, J. (2001). State of the art vibration isolation of large coordinate measuring machines with an adverse environment. In *Precision engineering nanotechnology (Turin, 27-31 May 2001)* (pp. 238-241).
72. Lorrain, P. (1974). Low natural frequency vibration isolator or seismograph. *Review of Scientific Instruments*, *45*(2), 198-202.
73. LaCoste, L. (1983). LaCoste and Romberg straight-line gravity meter. *Geophysics*, *48*(5), 606-610.
74. Veselago, V. G. (1968). " The Electrodynamics of Substances with Simultaneously Negative Values of and", Sov. Phys. Usp., vol. 10, pp. 509.
75. Smith, D. R., Padilla, W. J., Vier, D. C., Nemat-Nasser, S. C., & Schultz, S. (2000). Composite medium with simultaneously negative permeability and permittivity. *Physical review letters*, *84*(18), 4184.
76. Shelby, R. A., Smith, D. R., Nemat-Nasser, S. C., & Schultz, S. (2001). Microwave transmission through a two-dimensional, isotropic, left-handed metamaterial. *Applied Physics Letters*, *78*(4), 489-491.
77. Shelby, R. A., Smith, D. R., & Schultz, S. (2001). Experimental verification of a negative index of refraction. *science*, *292*(5514), 77-79.
78. Pendry, J. B. (2000). Negative refraction makes a perfect lens. *Physical review letters*, *85*(18), 3966.
79. Hashin, Z., & Shtrikman, S. (1962). On some variational principles in anisotropic and nonhomogeneous elasticity. *Journal of the Mechanics and Physics of Solids*, *10*(4), 335-342.
80. Berryman, J. G. (1980). Long-wavelength propagation in composite elastic media II. Ellipsoidal inclusions. *The Journal of the Acoustical Society of America*, *68*(6), 1820-1831.

81. Liu, Z., Zhang, X., Mao, Y., Zhu, Y. Y., Yang, Z., Chan, C. T., & Sheng, P. (2000). Locally resonant sonic materials. *science*, *289*(5485), 1734-1736.
82. Li, J., & Chan, C. T. (2004). Double-negative acoustic metamaterial. *Physical Review E*, *70*(5), 055602.
83. Zhou, X., Liu, X., & Hu, G. (2012). Elastic metamaterials with local resonances: an overview. *Theoretical and Applied Mechanics Letters*, *2*(4), 041001.
84. Saif, M. T. A. (2000). On a tunable bistable MEMS-theory and experiment. *Journal of microelectromechanical systems*, *9*(2), 157-170.
85. Kashdan, L., Seepersad, C., Haberman, M., & Wilson, P. S. (2009). Design, fabrication and evaluation of negative stiffness elements. In *Proceedings of the 20th Annual International Solid Freeform Fabrication Symposium*.
86. Yu, K., Fang, N. X., Huang, G., & Wang, Q. (2018). Magnetoactive acoustic metamaterials. *Advanced Materials*, *30*(21), 1706348.
87. Qiu, J., Lang, J. H., & Slocum, A. H. (2004). A curved-beam bistable mechanism. *Journal of microelectromechanical systems*, *13*(2), 137-146.
88. Hussein, H., Le Moal, P., Younes, R., Bourbon, G., Haddab, Y., & Lutz, P. (2019). On the design of a preshaped curved beam bistable mechanism. *Mechanism and Machine Theory*, *131*, 204-217.
89. Wang, Y. C., & Lakes, R. (2004). Negative stiffness-induced extreme viscoelastic mechanical properties: stability and dynamics. *Philosophical Magazine*, *84*(35), 3785-3801.
90. Prasad, J., & Diaz, A. R. (2005). Synthesis of Bistable Periodic Structures Using Topology Optimization and a Genetic Algorithm. *Journal of Mechanical Design*, *128(6)*, 1298–1306.

VITA

Jin Cui received his B.E. in Measuring & Controlling Technology and Instrument in June 2015 from Department of Precision Machinery and Instrumentation at University of Science and Technology of China (USTC) in Hefei, Anhui, China.

Jin Cui has research experiences in thermal interface materials, heat transfer measurements, micro-stereolithography and electroless metal plating. He also did some work in mechanical metamaterials.

PUBLICATIONS

Cui, J., Pan, L., & Weibel, J. A. (2020). Demonstration of a Compliant Microspring Array as a Thermal Interface Material for Pluggable Optoelectronic Transceiver Modules. *Journal of Electronic Packaging*, *142*(3).

Cui, J., Wang, J., Weibel, J. A., & Pan, L. (2019). A compliant microstructured thermal interface material for dry and pluggable interfaces. *International Journal of Heat and Mass Transfer*, 131, 1075–1082.

Zhong, M., **Cui, J.**, Hyun, J. S., Pan, L., Duan, P., & Zhang, S. (2019). Uniaxial 3D phase-shifting profilometry using a dual-telecentric structured light system in micro-scale devices. *Measurement Science and Technology*. Accepted Manuscript online 18 December.

Lu, C., Hu, Z. D., **Cui, J.**, Wang, J., & Pan, L. (2019). Strong light confinement and gradient force in parallel infinite-width monolayer graphene pairs. *Applied Physics Express*, *12*(7), 075007.

Cui, J., Pan, L., & Weibel, J. A. (2019). Demonstration of a Compliant Micro-Spring Array as a Thermal Interface Material for Pluggable Optoelectronic Transceiver Modules. In *International Electronic Packaging Technical Conference and Exhibition* (Vol. 59322, p. V001T02A004). American Society of Mechanical Engineers.

Cui, J., Wang, J., Zhong, Y., Pan, L., & Weibel, J. A. (2018). Metallized compliant 3D microstructures for dry contact thermal conductance enhancement. *Journal of Micromechanics and Microengineering*, 28(5), 055005.

Cui, J., Weibel, J. A., & Pan, L. (2018). Metallized Three-Dimensional Centrosymmetric Microstructures to Enhance Dry Contact Thermal Conductance across Nonflat Interfaces. *The 16th International Heat Transfer Conference (IHTC)*, IHTC16-23666.

Wasielewski, R., **Cui, J.**, Pan, L., & Weibel, J. A. (2016). Fabrication of compliant three-dimensional microstructures as surface coatings for dry contact thermal conductance enhancement. *2016 15th IEEE Intersociety Conference on Thermal and Thermomechanical Phenomena in Electronic Systems (ITherm)* (pp. 134–139).